JACS
ARTICLES
Published on Web 05/02/2007

Ab initio Study of Ultrafast Photochemical Reaction Dynamics of Phenol Blue

Takao Kobayashi,*[,†,‡] Motoyuki Shiga,[§] Akinori Murakami,[†,‡] and Shinichiro Nakamura[†,‡]

Contribution from the Mitsubishi Chemical Group Science and Technology Research Center, Inc., 1000 Kamoshida-cho, Aoba-ku, Yokohama 227-8502, Japan, CREST, Japan Science and Technology Agency (JST), Japan, and Center for Computational Science and E-systems, Japan Atomic Energy Agency, Higashi-Ueno 6-9-3, Taito-ku, Tokyo, 110-0015, Japan

Received September 29, 2006; E-mail: kobayashi.takao@ms.m-kagaku.co.jp

Abstract: Phenol blue (PB) is a primary skeletal structure part of indoaniline dyes and well-known as a solvatochromic dye. It has been recently observed by pump−probe (PP) transient absorption measurements that PB shows ultrafast ground state recovery within a few hundred femtoseconds after photoexcitation. In this work, the ultrafast photochemical reaction mechanism of PB has been investigated using direct *ab initio* (CASSCF) nonadiabatic molecular dynamics with the trajectory surface hopping (TSH) method. The swarm of trajectories starting from the S_1 Franck−Condon (FC) point has mostly shown surface hops (nonadiabatic transitions) from the S_1 state to the S_0 state at 110−120 fs in the vicinity of an S_1/S_0 conical intersection and after decay to the S_0 state bifurcated into two (Reverse and Forward) directions with almost the same branching ratio and reached the vicinity of the S_0 minimum energy point at 200−300 fs, which is in good agreement with the fast time component of the ground state recovery in the PP measurements. After reaching the vicinity of the S_0 minimum energy point, the trajectories showed a coherent vibration of bending motion between quinoneimine and aniline rings with a low frequency of 43 cm^{-1}, which presumably corresponds to a coherently photoexcitation-induced vibrational mode with a low frequency recently observed by the PP measurements.

1. Introduction

The elucidation of mechanisms of ultrafast photochemical processes is an essential subject for the control of photostabilities and photochemical reaction efficiencies of various organic materials as well as a rational design in molecular devices such as molecular switches or memories. The recent development of femtosecond spectroscopy has made it possible to follow time evolutions of ultrafast (femtosecond or subpicosecond) photochemical processes such as excited-state relaxations and chemical reactions from small molecules to biomolecules. In modern photochemistry,[1,2] it is considered that in the ultrafast photochemical reaction, the photoexcited molecule reaches the S_1 energy surface directly or via decay from an upper excited state and after that the reaction path evolves along a barrierless S_1 energy surface toward a conical intersection (CI), where internal conversion (nonadiabatic transition) occurs efficiently and the reaction path branches into some directions leading to different final products or back to the original reactant.

To understand the mechanisms of the photoinduced ultrafast processes in detail, interplay between experiments and theoretical calculations is indispensable. For obtaining realistic information of the photochemical reaction mechanism from the theoretical viewpoint, not only static calculations of excited-state potential energy surfaces (PESs) (i.e., geometry optimization of minimum energy points, transition states, and CIs and minimum energy paths (MEPs)), but also dynamic theoretical information (molecular dynamics calculation) is necessary, because a CI point that a photoexcited system meets depends on motions (momenta) of nuclei as well as a topology of PESs. Furthermore, to obtain reliable results, it is imperative to discuss the photochemical reaction mechanism based on PESs calculated by *ab initio* quantum chemical methods. The recent computer development has made it more and more realistic and practical to carry out picosecond-scale dynamical *ab initio* excited-state (direct molecular dynamics) calculations for medium-sized molecules as well as static *ab initio* excited-state calculations. However, there has been yet only a few reports on *ab initio* excited state (nonadiabatic) dynamics calculations for medium-sized molecules such as organic dyes.[3,4]

A solvatochromic dye,[5,6] phenol blue (PB) (4-[4-(dimethylamino)phenyl)imino]-2,5-cyclohexadien-1-one) is one of the

---

[†] Mitsubishi Chemical Group Science and Technology Research Center, Inc.

[‡] CREST-JST.

[§] Japan Atomic Energy Agency.

(1) Klessinger, M., Michl, J., Eds. *Excited States and Photochemistry of Organic Molecules*; VCH Publisher: New York, 1994.

(2) Olivucci, M., Ed. *Computational Photochemistry*; Theoretical and Computational Chemistry, Vol. 16; Elsevier: New York, 2005.

(3) Boggio-Pasqua, M.; Bearpark, M. J.; Hunt, P. A.; Robb, M. A. *J. Am. Chem. Soc.* **2002**, *124*, 1456−1470.

(4) Ko, C.; Levine, B. A. T.; Manohar, L.; Olsen, S.; Werner, H.-J.; Martinez, T. J. *J. Am. Chem. Soc.* **2003**, *125*, 12710−12711.

(5) Brooker, L. G. S.; Sprague, R. H. *J. Am. Chem. Soc.* **1941**, *63*, 3214−3215.

(6) McRae, E. G. *J. Phys. Chem.* **1957**, *61*, 562−572.

10.1021/ja066994w CCC: $37.00

Scheme 1

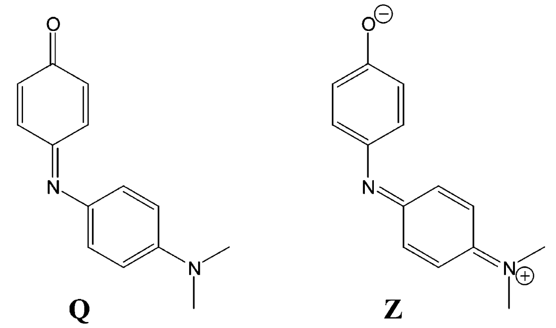

medium-sized organic dyes which shows ultrafast internal conversion from the excited-state to the ground state after photoexcitation. PB consists of an electron-donor (dimethylaniline) moiety (D) and an electron-acceptor (benzoquinone monoimine) moiety (A) with a π-conjugated bridge, shown in Scheme 1, and is a primary skeletal structure part of indoaniline dyes, which have been applied to cyan-colored materials in photography and dye diffusion thermal transfer (D2T2) printings. Therefore, from an industrial standpoint as well, it is very helpful to elucidate the photochemical or photophysical processes of PB as a model system of indoaniline dyes or their similar dyes with a quinoneimine chromophore such as indophenol or indonaphthol dyes.

PB has received continuous interests of experimental and theoretical chemists due to its interesting solvent effects on its stable (electronic) structure, several spectroscopic measurements, or potential for second-order nonlinear optical response materials.[7] The stable structure with an electronic character of the ground state of PB has been so far discussed from experimental and theoretical viewpoints.[8,9] As known in the case of the Brooker's merocyanine dyes,[10] in principle there is a possibility that the ground state of PB has two kinds of electronic structures described by two different extreme valence bond (VB) structures of the covalent quinoneimine type (**Q**) and the zwitterionic type (**Z**), shown in Scheme 1, each of which can have a different stable structure, and that which structure is more stable can be controlled by the polarity of surrounding solvents. Although Serrano et al.[8] suggested that PB exists as the **Q** structure in a nonpolar solvent and as the **Z** structure in a polar solvent from the MP2/STO-3G geometry optimization with INDO/S vertical excitation energy calculations, Morley et al.[9] excluded the possibility that diethylindoaniline exists as the **Z** structure in both protic and aprotic solvents by measuring NMR chemical shifts and suggested that PB exists only as the **Q** structure, which is also supported by their semiempirical molecular orbital (AM1 and PM3) calculations considering solvent effects with a dielectric continuum solvation model (COSMO).

The first electric dipole allowed excited state of PB is mainly characterized by an electron-transfer (ET) structure from D(π(HOMO)) to A(π^*(LUMO)), where the VB weight of the **Z** structure increases. The excitation from the ground state to that ET excited state enhances the permanent electric dipole moment and causes the wavelength of the absorption maximum to be longer as the solvent polarity increases (*bathochromism* or *positive solvatochromism*).[5,6,9,11,12] The positive solvatochromism of PB is also considered to be caused by hydrogen bonds with protic solvents.[6,9,11,12] There have been some theoretical calculations reported on the solvatochromism of PB, that is, the solvent dependence of vertical excitation energies, by using semiempirical molecular orbital calculations considering the solvent effects with the dielectric continuum solvation model.[8,9,13,14] Although the semiempirical INDO/S with a self-consistent reaction field (SCRF) model calculations suggested that the lowest vertical singlet excited (S_1) state is $n(O) \rightarrow \pi^*$(LUMO) state in the gas phase (or nonpolar solvents) and can be changed to π(HOMO)$\rightarrow\pi^*$(LUMO) state in polar solvents, the identification of the character of vertical S_1 state remains controversial and to be reinvestigated by highly accurate methods such as *ab initio* quantum chemical (or density functional theory (DFT)) calculations including the dynamical electron correlation effect. The solvation effects on spectroscopic spectra of PB have been also observed on nonresonance and resonance Raman shifts of the $C{=}N$ and $C{=}O$ stretching modes.[15−18]

Recently, some experimental studies on photoexcitation dynamics of PB have been done by measuring the pump−probe (PP) transient absorption spectroscopy in several solvents. Kimura et al.[19] surveyed the entire transient absorption spectral range from 500 to 850 nm with a time resolution of about 200 fs, whereas Nagasawa et al.[20] probed the ground state recovery only at 635 nm with a much higher time resolution of 30 fs. In both experiments, fast and slow decay components have been detected. Kimura et al. observed the fast decay component of 0.5 ps and the slow one of 10 ps, whereas Nagasawa et al. observed the fast decay components of 0.22−0.37 ps and slow one of 10−15 ps. Both of them have assigned the faster time constant to the life time of the excited state and the slower one to the ground state dynamics including solvation dynamics, vibrational cooling, and/or structural relaxation. Furthermore, in the PP spectroscopy with a high time resolution by Nagasawa et al.[20] coherently photoexcitation-induced vibrational modes with a very low frequency of 70 cm^{-1} in aprotic solvents and that of 100 cm^{-1} in protic solvents were observed. They have suggested that the low-frequency mode might be due to an intermolecular solvation mode. On the other hand, the theoretical investigation of the mechanism of the ultrafast photochemical reaction dynamics of PB even in the gas phase has never been performed and it remains to be done.

The objective of the current study is to obtain insight into the mechanism of the ultrafast photochemical reaction of PB

---

(7) Marder, S. R.; Beratan, D. N.; Cheng, L.-T. *Science* **1991**, *252*, 103−106.
(8) Serrano, A.; Canuto, S. *Int. J. Quantum Chem.* **1998**, *70*, 745−750.
(9) Morley, J. O.; Fitton, A. L. *J. Phys. Chem. A* **1999**, *103*, 11442−11450.
(10) Morley, J. O.; Morley, R. M.; Docherty, R.; Charlton, M. H. *J. Am. Chem. Soc.* **1997**, *119*, 10192−10202.
(11) Figueras, J. *J. Am. Chem. Soc.* **1971**, *93*, 3255−3263.
(12) Kolling, O. W. *Anal. Chem.* **1978**, *50*, 212−215.
(13) Karelson, M. M.; Zerner, M. C. *J. Phys. Chem.* **1991**, *96*, 6949−6957.
(14) Luzhkov, V.; Warshel, A. *J. Am. Chem. Soc.* **1991**, *113*, 4491−4499.
(15) Yamaguchi, T.; Kimura, Y.; Hirota, N. *J. Phys. Chem. A* **1997**, *101*, 9050−9060.
(16) Yamaguchi, T.; Kimura, Y.; Hirota, N. *J. Chem. Phys.* **1998**, *109*, 9075−9083.
(17) Yamaguchi, T.; Kimura, Y.; Hirota, N. *J. Chem. Phys.* **1998**, *109*, 9084−9095.
(18) Terenziani, F.; Painelli, A.; Comoretto, D. *J. Phys. Chem. A* **2000**, *104*, 11049−11054.
(19) Kimura, Y.; Yamaguchi, T.; Hirota, N. *Phys. Chem. Chem. Phys.* **2000**, *2*, 1415−1420.
(20) Nagasawa, Y.; Watanabe, A.; Ando, Y.; Okada, T. *J. Mol. Liquids* **2001**, *90*, 295−302.

Chart 1

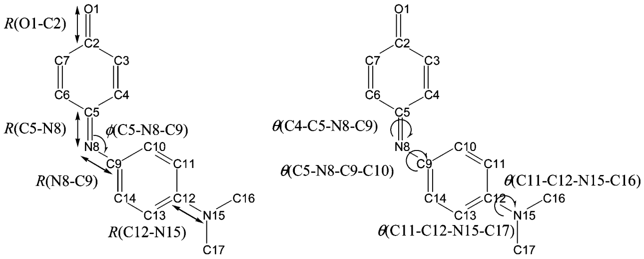

in vacuum (i.e., in the gas phase) through *ab initio* quantum chemical calculations (mainly at the CASSCF level[21,22]). The mechanism has been investigated by static and dynamic approaches: In the static calculations, we have confirmed that the π(HOMO)→π^*(LUMO) S$_1$ state with the **Z**-like character and the S$_0$ state with the **Q** character are relevant to the photochemical reaction and verified static ultrafast photochemical reaction paths by calculating MEPs starting from the S$_1$ Franck-Condon (FC) point and a minimum energy point of S$_1$/S$_0$ CI (S$_1$/S$_0$ CImin), which has been found to be a branching point by the calculations of the MEPs from the CI. For obtaining the dynamical information, direct semiclassical nonadiabatic molecular dynamics computations starting from the S$_1$ FC point were carried out by means of the trajectory surface hopping (TSH) method, in which the *ab initio* CASSCF energies, gradients, and nonadiabatic coupling vectors were used. The trajectories obtained by the TSH nonadiabatic dynamics simulation starting from the S$_1$ FC state has mostly shown nonadiabatic transitions to the ground state around 110−120 fs and reached the vicinity of the S$_0$ minimum energy point around 200−300 fs. This is in good agreement with the fast time component of ground state recovery time observed by the PP spectroscopy in solvents.[20] Furthermore, after decay to the ground state, the trajectories showed a coherent vibration of bending motion between quinoneimine and aniline rings with a low frequency of 43 cm^{-1}, which presumably corresponds to a coherently photoexcitation-induced vibrational mode with a low frequency observed by the PP measurements.[20]

2. Computational Methods

As shown in Chart 1, the carbon, nitrogen, and oxygen atoms are numbered and structural parameters are defined. R, ϕ, and θ denote bond lengths, bond angles, and dihedral angles, respectively. The ground state (S$_0$) of PB has two global minimum (S$_0$min) points which are equivalent in energy and mirror images to each other. The dihedral angle θ(C5−N8−C9−C10) of one S$_0$min is between −90° and 0°, whereas that of the other is between 0° and 90°. We call the former "S$_0$min(R)" and the latter "S$_0$min(L)". Hereafter, S$_0$min denotes S$_0$min(R) unless specified. For convenience in describing the photochemical reaction dynamics, we define cis/trans forms of PB by distinguishing the C4 and C6 atoms, which are equivalent in reality, and define a form of PB with θ(C4−C5−N8−C9) ≈ 0° as "cis" and that with θ(C4−C5−N8−C9) ≈ 180° as "trans". The cis/trans and R/L forms of S$_0$min of PB are shown in Chart S1 of the Supporting Information (SI). In reality, S$_0$min(cis/L) and S$_0$min(cis/R) are equivalent to S$_0$min(trans/L) and S$_0$min(trans/R), respectively, because the C4 and C6 atoms cannot be distinguished.

For all the calculations carried out in this study, we employed the *ab initio* state-averaged(SA)-CASSCF method in which the active space consists of two active orbitals of HOMO (ϕ_{HOMO}) and LUMO(ϕ_{LUMO}) (shown in Figure 1) and two active electrons, and two states (S$_0$ and S$_1$) are included in the average with equal weights, which is denoted as SA2-CASSCF(2,2).

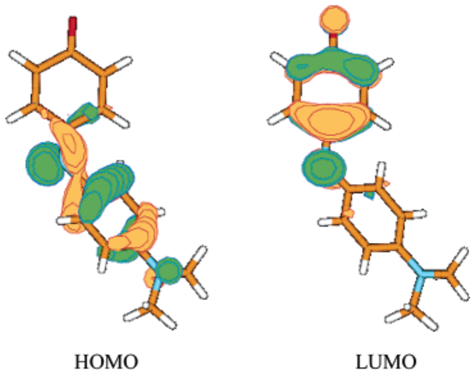

Figure 1. HOMO and LUMO used as active orbitals in the SA2-CASSCF-(2,2)/6-31G* calculation.

2.1. Static Calculations. We have performed the static calculations on PB in vacuum (i.e., in the gas phase) as follows:

- S$_0$min structure, vertical excitation energies, and permanent electric dipole moments
- Optimization of an S$_1$/S$_0$ conical intersection (CI) structure and characterization of the minimum energy point of S$_1$/S$_0$ CI (S$_1$/S$_0$ CImin)
- Minimum energy paths (MEPs)
  − On the S$_1$ potential energy surface (PES) starting from the S$_1$ Franck-Condon (FC) point
  − On the S$_0$ PES starting from the S$_1$/S$_0$ CImin point

For the S$_0$ geometry optimization and the calculations of vertical excitation energies and permanent electric dipole moments, several quantum chemical or density functional theory (DFT) methods including the dynamical electron correlation effect were used as well as the SA2-CASSCF(2,2) method to check the accuracy of the SA2-CASSCF(2,2) calculations. The electron correlated methods used for the S$_0$ geometry are the second-order Møller-Plesset perturbation theory (MP2) and the DFT with Becke 3 parameters Lee-Yang-Parr hybrid xc-functional (B3LYP).[23] To evaluate the accuracy of the calculated S$_0$min structures of PB, it is necessary to compare the calculated structures with an experimental one. Although there have been no experimental data reported on the PB structure, instead there is an indoaniline-derived calix[4]arene the structure of which was experimentally measured by an X-ray crystallography[24] and available in the Cambridge Structural Database (Refcode TEYGOT), shown in Chart 2. The indoaniline-derived calix[4]arene is called TEYGOT in this paper. To assess the accuracy of methodologies used for the ground state calculations of PB, it is expected to be reasonable to use TEYGOT including the PB skeletal structure as an experimental reference instead of PB. We performed the calculations of the S$_0$min structures of TEYGOT at the Hartree−Fock (HF), MP2, and B3LYP levels, which are compared with the X-ray structure. For the calculations of vertical excitation energies and permanent electric dipole moments, we used the multi-state multireference second-order Møller-Plesset perturbation theory using the SA2-CASSCF(2,2) wavefunction as a zeroth-order wavefunction (MS-CAS(2,2)PT2[25,26]) and time-dependent DFT with B3LYP hybrid xc-functional (TDDFT(B3LYP)).[27] In addition, the vertical excitation energies were also calculated at the symmetry adapted cluster config-

---

(21) Werner, H.-J.; Knowles, P. J. *J. Chem. Phys.* **1985**, *82*, 5053.

(22) Knowles, P. J.; Werner, H.-J. *Chem. Phys. Lett.* **1985**, *115*, 259−267.

(23) Stephens, P. J.; Devlin, F. J.; Chabalowski, C. F.; Frisch, M. J. *J. Phys. Chem.* **1994**, *98*, 11623−11627.

(24) Kubo, Y.; Tokita, S.; Kojima, Y.; Osano, Y. T.; Matsuzaki, T. *J. Org. Chem.* **1996**, *61*, 3758−3765.

(25) Andersson, K.; Malmqvist, P.-Å.; Roos, B. O.; Sadlej, A.; Wolinski, K. *J. Phys. Chem.* **1990**, *94*, 5483.

(26) Andersson, K.; Malmqvist, P.-Å.; Roos, B. O. *J. Chem. Phys.* **1992**, *96*, 1218.

(27) Casida, M. E. In *Recent Advances in Density Functional Methods*; Chong, D. P., Ed.; World Scientific: Singapore, 1995.

Chart 2

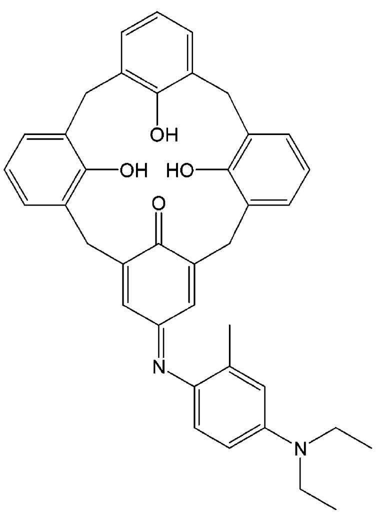

uration interaction (SAC-CI) level.[28] The permanent electric dipole moments were calculated by numerical differentiation of energies with respect to static electric field strengths (finite-field method). Furthermore, to examine a solvent effect on the (electronic) structure and excitation energies, we have also performed the B3LYP and TDDFT-(B3LYP) calculations using the polarizable continuum solvation model (PCM)[29] (PCM-B3LYP and PCM-TDDFT(B3LYP)[30]).

S_1/S_0 CImin was calculated at the SA2-CASSCF(2,2) level and characterized by the topography in the branching plane using conical parameters derived from the degenerate perturbation theory proposed by Yarkony.[31,32] The SA2-CASSCF(2,2) MEPs calculations were performed on the S_1 surface starting from the S_1 FC point (S_0min(cis/R)) and on the S_0 surface starting from the S_1/S_0 CImin point. Points located at every 10 degrees along a circle centered at the S_1/S_0 CImin with radius $\rho = 0.01$ amu$^{1/2}$*bohr in the branching plane were chosen as starting points of the MEPs calculations on the S_0 surface from the S_1/S_0 CImin.

With respect to basis sets, for the calculations of the S_0min structure, the vertical excitation energies, the permanent electric dipole moments, and the S_1/S_0 CImin structure we employed both 6-31G* and 6-31G augmented with d polarization functions on the nitrogen and oxygen atoms (denoted as 6-31G(d on N/O)) in which 6d type of d functions were used. The characterization of S_1/S_0 CImin and the MEPs calculations were performed using only the 6-31G(d on N/O) basis set.

The SA2-CASSCF(2,2) optimizations of the S_0 and S_1/S_0 CI structures and the SA2-CASSCF(2,2) calculations of the vertical excitation energies were carried out using MOLPRO2002.[33] For the MS-CAS(2,2)PT2 and MEPs calculations, MOLCAS6[34] was used. The Hartree−Fock (HF), MP2, and (PCM-)B3LYP optimization of the S_0 geometry and the (PCM-)TDDFT(B3LYP) and SAC-CI vertical excitation energies were calculated using Gaussian03.[35]

2.2. Dynamics Calculations. Semiclassical nonadiabatic molecular dynamics calculations in the full space of coordinates, where the nuclei are treated classically and the electrons are described quantum mechanically, were performed using the trajectory surface hopping (TSH) method with the Tully's fewest switches algorithm,[36] in which an adiabatic representation was chosen. The dynamics computations were carried out using a direct method. The (adiabatic potential) energies, gradients, and nonadiabatic coupling (NADC) vectors needed in the dynamics calculations were computed at the SA2-CASSCF(2,2)/6-31G(d on N/O) level "on the fly" at each point on the trajectory by using MOLPRO2002.[33] The procedure of semiclassical nonadiabatic molecular dynamics calculation is outlined below.

Step 1: Initial conditions at an initial time $t_0 = 0$ are assigned. Initial position $\mathbf{R}(t_0)$ and momentum $\mathbf{P}(t_0)$ (or velocity $\dot{\mathbf{R}}(t_0)$) of all the atoms are set to be the S_0min(cis/R) (S_1 FC) point and zero, respectively. An initial electronic state is assigned to a pure adiabatic electronic S_1 state, where time-varying complex-valued expansion coefficients of a full electronic wavefunction expanded by adiabatic S_1 and S_0 state wavefunctions $c_1(t_0)$ and $c_0(t_0)$ are given by 1.0 and 0.0, respectively. (Hereafter, subscripts 1 and 0 denote the S_1 and S_0 states, respectively.) An initial time step Δt_0 for integrating the classical mechanical equation of motions for the atoms was chosen as 20.0 au ($\approx$0.484 fs), which is adjusted as explained below. A maximum time step Δt_{max} is set as 20.0 au.

Step 2: At an initial position $\mathbf{R}(t_0)$, the calculations of adiabatic S_1 and S_0 electronic wavefunctions were performed at the SA2-CASSCF-(2,2) level to obtain energies, gradients, and nonadiabatic coupling (NADC) vectors $\mathbf{d}_{ij}(t_0)$ ($i, j = 0, 1$).

Step 3: The classical mechanical Newton's equations of motions for the atoms on the current PES are integrated from the current time t to $t + \Delta t$ by using the velocity Verlet algorithm to obtain a new position $\mathbf{R}(t + \Delta t)$ and momentum $\mathbf{P}(t + \Delta t)$.

Step 4: At a new position $\mathbf{R}(t + \Delta t)$, the SA2-CASSCF(2,2) calculations of energies, gradients, and nonadiabatic coupling vectors are carried out. The signs of the NADC vectors might be unexpectedly reversed due to accidental changes of the phases (plus or minus) of adiabatic S_1 and S_0 wavefunctions in a trajectory calculation. To ensure the continuity of the NADC vectors, the phases of S_1 and S_0 wavefunctions at a current step are determined to be consistent with those at a previous step and the signs of the NADC vectors are also determined in association with the changes of the phases of S_1 and S_0 wavefunctions between steps. The nonadiabatic coupling region between adiabatic electronic states are possibly quite local and change dramatically in the vicinity of conical intersections, where the adiabatic electronic wavefunctions change dramatically with strong mutual mixtures. Therefore, the time step for propagating the motions of atoms in a nonadiabatic coupling region should be adjusted to be short enough for the adiabatic electronic wavefunctions to change only slightly between steps. This is achieved by the following method. If an overlap of an S_1 configuration interaction (ConfI) vector at a previous step and that at a current step is less than 0.99 or an overlap of an S_1 ConfI vector at a previous step and an S_0 ConfI vector at a current step is larger than 0.10, then the time step for propagating the motions of atoms is adjusted as $\Delta t = \Delta t/1.2$ and return to Step 3 without any updates of the position $\mathbf{R}(t)$ and momentum $\mathbf{P}(t)$. Otherwise, it is increased as $\Delta t = \Delta t \times 1.2$, unless $\Delta t \times 1.2$ is larger than Δt_{max} and adopts a new updated position $\mathbf{R}(t + \Delta t)$ and momentum $\mathbf{P}(t + \Delta t)$, then go to Step 5.

Step 5: The equations for the electronic expansion amplitudes of the S_1 and S_0 states are integrated from $c_i(t)$ to $c_i(t + \Delta t)$ ($i = 0, 1$) using a time step of $\delta t (= \Delta t/1000)$ by diagonalizing the 2×2 matrix $A_{ij}(= E_i\delta_{ij} - i\hbar\dot{\mathbf{R}}\cdot\mathbf{d}_{ij}$, where E_i is an adiabatic potential energy for an electronic state i), whereas the velocities of atoms and the NADC vectors are kept fixed at $\dot{\mathbf{R}}(t)$ and $\mathbf{d}_{ij}(t)$, respectively, from t to $t + \Delta t$ based on the multiple time scale algorithm.

Step 6: The switching probability g_{ij} ($i, j = 0, 1$) from the current electronic state i to another state j is calculated.

---

(28) Nakatsuji, H. *Chem. Phys. Lett.* **1978**, *59*, 362−364.
(29) Tomasi, J.; Persico, M. *Chem. Rev.* **1994**, *94*, 2027−2094.
(30) Scalmani, G.; Frisch, M. J.; Mennucci, B.; Tomasi, J.; Cammi, R.; Barone, V. *J. Chem. Phys.* **2006**, *124*, 094107.
(31) Yarkony, D. R. *J. Phys. Chem. A* **2001**, *105*, 6277−6293.
(32) Domcke, W., Yarkony, D. R., Köppel, H., Eds. *Conical Intersections*; Advanced Series in Physical Chemistry, Vol. 15; World Scientific: Singapore, 2004.
(33) Werner, H.-J.; et al. *MOLPRO*, version 2002.6, a package of ab initio programs; 2003; see http://www.molpro.net.
(34) Karlström, G.; Lindh, R.; Malmqvist, P.-Å.; Roos, B. O.; Ryde, U.; Veryazov, V.; Widmark, P.-O.; Cossi, M.; Schimmelpfennig, B.; Neogrady, P.; Seijo, L. *Comput. Mater. Sci.* **2003**, *28*, 222.
(35) Frisch, M. J.; et al. *Gaussian 03*, revision C.02; Gaussian, Inc.: Wallingford, CT, 2004.
(36) Tully, J. C. *J. Chem. Phys.* **1990**, *93*, 1061−1071.

Step 7: A uniform random number between 0 and 1 is generated, and whether a switch from a current state to another state should be invoked is determined by comparing the switching probabilities with the generated random number.

Step 8: If no switch occurs, go back to Step 3. If a switch from a current state to another state occurs, adjustment of the component of velocity in the direction of the NADC vector is made at a current position to conserve total energy, which is justified by semiclassical theory.[37] If the required velocity reduction is greater than the component of velocity to be adjusted, no switch occurs without any changes of velocity and go back to Step 3. Otherwise, after the velocity adjustment has been made, a switch from a current state to another state is invoked, and return to Step 3.

This procedure is repeated until a trajectory reaches a given finishing time. One-hundred independent trajectories are run for sampling until it can be determined into which direction they bifurcate after surfaces hops. This sampling includes only the ensemble average over the trajectories which stochastically undergoes surface hops (nonadiabatic transitions) and does not include the average over initial configurations, that is, only one position (= S_0min) with one momentum (= 0) was employed as an initial configuration, as explained above. Four trajectories are run for two picoseconds to investigate longer time scale dynamics after the decay to the ground state.

3. Results and Discussion

This section is divided into five subsections. In subsection 3.1, we show the optimized structure of the S_0min point and examine the characters of three lowest singlet FC states. In subsection 3.2, the optimized structure of the S_1/S_0 CImin point is presented and its characterization is discussed. In subsection 3.3 and 3.4, we investigate and analyze static reaction pathways (MEP) starting from the S_1 FC and S_1/S_0 CImin points. In subsection 3.5, semiclassical nonadiabatic dynamics calculations starting from the S_1 FC point are discussed.

3.1. S_0min Structure, Vertical Excitation Energies, and Permanent Electric Dipole Moments. Before discussions about photochemical reaction paths of PB, we will assess how well the SA2-CASSCF(2,2) level of calculation can describe the ground state by comparing the S_0min structure at the SA2-CASSCF(2,2) level with those at the levels including dynamical electron correlation effects and an X-ray crystallographic structure. Table 1 shows the S_0min structures of PB optimized at the SA2-CASSCF(2,2) level compared with those at the HF, MP2, and B3LYP levels. In Table 2, the optimized S_0 structures of the indoaniline part of TEYGOT at the HF, MP2, and B3LYP levels are shown with the X-ray crystallographic structure. Because in the calculated S_0min structures there are no significant differences between the results by 6-31G* and 6-31G(d on N/O) basis sets, we refer the structures calculated by 6-31G* unless specified.

Table 1. Optimized S_0min Structures of Phenol Blue[a]

parameter	SA2-CASSCF(2,2)	HF	MP2	B3LYP
R(O1−C2)	1.197	1.197	1.241	1.232
	1.206	1.206	1.252	1.240
R(C5−N8)	1.270	1.264	1.315	1.307
	1.277	1.269	1.318	1.312
R(N8−C9)	1.392	1.406	1.398	1.384
	1.395	1.410	1.411	1.390
R(C12−N15)	1.387	1.391	1.394	1.380
	1.392	1.397	1.404	1.385
ϕ(C5−N8−C9)	126.03	124.29	120.75	125.05
	125.17	123.77	121.02	124.46
θ(C4−C5−N8−C9)	−10.11	−5.88	−10.34	−11.92
	−10.35	−6.33	−9.44	−12.09
θ(C5−N8−C9−C10)	−38.02	−51.49	−46.14	−36.19
	−37.19	−49.65	−47.21	−35.68
θ(C11−C12−N15−C16)	−12.26	−13.66	−16.59	−3.83
	−14.23	−15.90	−16.78	−7.86
θ(C11−C12−N15−C17)	−164.04	−163.63	−160.88	−172.92
	−162.19	−161.71	−160.99	−169.48

[a] Bond lengths are given in Å and the bond and dihedral angles are in degrees. (See Chart 1 for the notations of the structural parameters.) The upper and lower values are calculated by using the 6-31G* and 6-31G(d on N/O) basis sets, respectively.

Table 2. Optimized S_0 Structures of the Indoaniline Part of TEYGOT[a]

parameter	HF	MP2	B3LYP	expt.
R(O1−C2)	1.205		1.256	1.302
	1.214	1.264	1.265	
R(C5−N8)	1.265		1.316	1.334
	1.271	1.327	1.322	
R(N8−C9)	1.405		1.370	1.366
	1.407	1.398	1.375	
R(C12−N15)	1.384		1.377	1.350
	1.385	1.391	1.380	
ϕ(C5−N8−C9)	124.58		125.97	125.83
	124.15	121.41	125.27	
θ(C4−C5−N8−C9)	−7.09		−13.97	−12.39
	−7.77	−11.92	−14.43	
θ(C5−N8−C9−C10)	−49.67		−32.55	−24.71
	−47.21	−42.97	−31.97	
θ(C11−C12−N15−C16)	7.91		3.28	6.51
	2.28	−1.98	2.39	
θ(C11−C12−N15−C17)	−169.15		−173.64	−180.54
	−174.21	−171.44	−174.00	

[a] Bond lengths are given in Å and the bond and dihedral angles are in degrees. (See Chart 1 for the notations of the structural parameters.) The upper and lower values are calculated by using the 6-31G* and 6-31G(d on N/O) basis sets, respectively.

First we note the S_0min structure calculations of TEYGOT. In comparison with the X-ray crystallographic data, the B3LYP S_0min structure of TEYGOT is closer to the X-ray structure than the MP2 one (in the case of using the 6-31G(d on N/O) basis set), especially in R(N8−C9), ϕ(C5−N8−C9), and θ(C5−N8−C9−C10). However, there are still small discrepancies between the B3LYP and X-ray structures of TEYGOT: Compared with the X-ray data (R(O1−C2) = 1.302 Å, R(C12−N15) = 1.350 Å, and θ(C5−N8−C9−C10) = −24.71°), the B3LYP values of R(O1−C2)(1.256 Å) and R(C12−N15)(1.377 Å) are 0.046 Å shorter and 0.027 Å larger, respectively, and the B3LYP value of θ(C5−N8−C9−C10)(−32.55°) is 7.84° larger in magnitude. This means that the S_0 electronic structure of TEYGOT at the B3LYP level includes less **Z** character than that in the real single crystal. Nonetheless compared with the HF structure (R(N8−C9) = 1.405 Å, R(C12−N15) = 1.384 Å, θ(C4−C5−N8−C9) = −7.09°, and θ(C5−N8−C9−C10) = −49.67°), the B3LYP values of R(N8−C9) and R(C12−N15) are 0.035 Å and 0.007 Å shorter and the B3LYP values of θ(C4−C5−N8−C9) and θ(C5−N8−C9−C10) are 6.88° larger and 17.12° smaller in magnitude, respectively, which is considered to be caused by an increase of the **Z** character in the S_0 electronic structure by an electron correlation effect.

Next we note the calculated S_0min structures of PB. Considering the similarity to the case of TEYGOT, the B3LYP structure of PB in vacuum is expected to be more reliable than the MP2 one. Therefore, in the calculations of the vertical excitation energies and permanent electric dipole moments of

---

(37) Tully, J. C. *Int. J. Quantum Chem. Symp.* **1991**, *25*, 299−309.

Table 3. Vertical Excitation Energies (eV) and Oscillator Strengths from the S_0 State to Three Lowest Singlet Franck−Condon Excited States of Phenol Blue[a]

		vertical excitation energy (eV)					oscillator strength			
state	character	SA2-CAS-SCF(2,2)[b]	MS-CAS-(2,2)PT2[c]	TDDFT (B3LYP)	SAC-CI (level2)	expt.	SA2-CAS-SCF(2,2)[b]	MS-CAS-(2,2)PT2[c]	TDDFT (B3LYP)	SAC-CI (level2)
S_1	π(HOMO)→π*(LUMO)	3.38	2.15	2.33	2.27	2.16[d], 2.25[e]	0.89	0.57	0.39	0.34
		(3.72)	(2.28)				(0.63)	(0.39)		
		3.45	2.23	2.36	2.37		0.92	0.60	0.39	0.37
		(3.77)	(2.40)				(0.66)	(0.42)		
S_2	n(O)→π*(LUMO)			2.57	2.76				0.02	0.01
				2.52	2.80				0.06	0.01
S_3	n(N)→π*(LUMO)			3.50	3.90				0.15	0.22
				3.51	3.91				0.14	0.21

[a] S_0min geometry optimized at the B3LYP/6-31G*(or 6-31G(d on N/O)) level was used. The upper and lower calculated values are obtained by using the 6-31G* and 6-31G(d on N/O) basis sets, respectively. [b] Numbers in parentheses were calculated at the SA2-CASSCF(2,2) S_0min point. The SA2-CASSCF(2,2) S_0 energies at the B3LYP S_0 min point are −722.004699 au by 6-31G* and −721.777716 au by 6-31G(d on N/O). The SA2-CASSCF(2,2) S_0 energies at the SA2-CASSCF(2,2) S_0min point are −722.012345 au by 6-31G* and −721.785671 au by 6-31G(d on N/O). [c] MS-CAS(2,2)PT2 ocsillator strengths were calculated by using SA2-CASSCF(2,2) transition moments and MS-CAS(2,2)PT2 energies. Numbers in parentheses were calculated at the SA2-CASSCF(2,2) S_0min point. The MS-CAS(2,2)PT2 S_0 energies at the B3LYP S_0min point are −724.374139 au by 6-31G* and −723.566401 au by 6-31G(d on N/O). The MS-CAS(2,2)PT2 S_0 energies at the SA2-CASSCF(2,2) S_0min point are −724.365516 au by 6-31G* and −723.553208 au by 6-31G(d on N/O). [d] Measured in benzene by Kimura et al.[19] and Nagasawa et al.[20] [e] Measured in cyclohexane by Brooker et al.[5]

PB, we employed the B3LYP S_0min structure. The SA2-CASSCF(2,2) structure of PB is considerably close to the B3LYP one, although the SA2-CASSCF(2,2) R(O1−C2) and R(C5−N8) are shorter than the B3LYP ones. The discrepancy between the SA2-CASSCF(2,2) and B3LYP structures may be mainly due to a dynamical electron correlation effect. We consider that a nondynamical electron correlation effect included by the SA2-CASSCF(2,2) method is important to describe the S_0 electronic structure.

Table 3 shows the vertical excitation energies and oscillator strengths from the S_0 state to three lowest singlet Franck-Condon (FC) excited states in vacuum at the SA2-CASSCF-(2,2), MS-CAS(2,2)PT2, TDDFT(B3LYP), and SAC-CI levels with experimental absorption maximum of the visible absorption band in nonpolar solvents (benzene[19,20] and cyclohexane[5]). Because in the calculated vertical excitation energies and oscillator strengths there are no significant differences between the results by 6-31G* and 6-31G(d on N/O) basis sets, we refer the calculated values by 6-31G*. The SA2-CASSCF(2,2) value (3.38 eV) of the vertical excitation energy to the π(HOMO)→π*(LUMO) state is more than 1 eV larger than experimental values, which is quite well improved by including a dynamical electron correlation effect by the MS-CAS(2,2)-PT2 method. As shown in Figure 1, HOMO and LUMO are clearly localized on the aniline ring and the quinoneimine ring, respectively, so that the π(HOMO)→π*(LUMO) state is characterized as an electron transfer state from the aniline ring to the quinoneimine one and has the **Z**-like electronic structure. Furthermore, the MS-CAS(2,2)PT2 value (2.15 eV) of the vertical excitation energy to the π(HOMO)→π*(LUMO) state is close to the TDDFT(B3LYP)(2.33 eV) and SAC-CI(level2)-(2.27 eV) values, which are near to experimental results (2.16 eV in benzene and 2.25 eV in cyclohexane). It is concluded from the TDDFT(B3LYP) and SAC-CI(level2) calculations of the vertical excitation energies and the oscillator strengths that the S_1, S_2, and S_3 FC states of PB in vacuum have the π(HOMO)→π*(LUMO), n(O)→π*(LUMO), and n(N)→π*(LUMO) characters, respectively, and that vertical transitions to the S_1(π(HOMO)→π*(LUMO)) and S_3 (n(N)→π*(LUMO)) FC states are allowed whereas that to S_2(n(O)→π*(LUMO)) FC state is almost forbidden.

Table 4. Calculated Averaged Permanent Electric Dipole Moment (Debye) of Phenol Blue[a]

state	character	SA2-CASSCF(2,2)	MS-CAS(2,2) PT2	TDDFT (B3LYP)
S_0[b]		7.07	8.08	8.35
		7.47	7.74	8.74
S_1	π(HOMO) → π*(LUMO)	15.16	13.33	12.05
		15.72	14.26	11.95
S_2	n(O) → π*(LUMO)			4.65
				5.56
S_3	n(N) → π*(LUMO)			12.49
				12.75

[a] $\mu_{av} = \sqrt{\mu_x^2+\mu_y^2+\mu_z^2}$. The upper and lower calculated values are obtained by using the 6-31G* and 6-31G(d on N/O) basis sets, respectively. The geometry optimized at the B3LYP/6-31G* (or 6-31G(d on N/O)) level was used. [b] Experimental value of $\mu_{av}(S_0)$ is 5.8 Debye.[5]

Now we consider a possibility that the character of the S_1 FC (π(HOMO)→π*(LUMO)) state interchanges with that of another FC state in polar solvents. Table 4 shows the averaged permanent electric dipole moments (μ_{av}) of PB in vacuum calculated at the SA2-CASSCF(2,2), MS-CAS(2,2)PT2, and TDDFT(B3LYP) levels with the 6-31G* and 6-31G(d on N/O) basis sets. The MS-CAS(2,2)PT2 and TDDFT(B3LYP) μ_{av} values of the S_0 and S_1 FC states are comparable with each other and about 1.0 Debye larger for the S_0 state and about 2.0−3.0 Debye smaller for the S_1 FC state than the SA2-CASSCF(2,2) value; that is, the dynamical electron correlation effect increases the μ_{av} value of the S_0 state and decreases that of the S_1 FC state. This means that the dynamical electron correlation effect mixes the S_0 electronic structure mainly having **Q** character with the S_1 electronic structure having **Z**-like character and vice versa, which is reflected in the S_0 optimized structures as shown above. On the other hand, the experimental μ_{av} value of the S_0 state in benzene reported very early,[5] which indicates a balance of mixing between the **Q** and **Z** structures of the S_0 state, is 5.8 Debye, which is about 2 Debye smaller than the MS-CAS(2,2)PT2 and B3LYP values. Because there is a possibility that the DFT with the B3LYP functional might overestimate dipole moments of charge-transfer systems due to a self-interaction error,[38] further discussions are necessary to understand the discrepancies between the theoretical and

---

(38) Prezhdo, O. V. *Adv. Mater.* **2002**, *14*, 597−600.

experimental values of the μ_{av} value of the S_0 state. However, from the comparison with the X-ray crystallographic structure, as shown above, and very good agreement between vibrational frequencies of the O1−C2(C═O) and C5−N8(C═N) stretching modes calculated at the PCM-B3LYP level and those observed by experimantal Raman shifts, as will be shown later, the B3LYP calculations is considered to describe the S_0 electronic structure of PB very well.

The TDDFT(B3LYP) calculations (in vacuum) show that the order of μ_{av} for the S_0−S_3 FC states is $\mu_{\mathrm{av}}(S_3(n(N)\rightarrow\pi^*(\mathrm{LUMO}))) \approx \mu_{\mathrm{av}}(S_1(\pi(\mathrm{HOMO})\rightarrow\pi^*(\mathrm{LUMO}))) > \mu_{\mathrm{av}}(S_0) > \mu_{\mathrm{av}}(S_2(n(O)\rightarrow\pi^*(\mathrm{LUMO})))$, which indicates that the $S_1(\pi(\mathrm{HOMO})\rightarrow\pi^*(\mathrm{LUMO}))$ FC state would be stabilized in polar solvents as much as the $S_3(n(N)\rightarrow\pi^*(\mathrm{LUMO}))$ FC state and more than the $S_2(n(O)\rightarrow\pi^*(\mathrm{LUMO}))$ FC state. Therefore, it is expected that the S_1 FC state remains to have the $\pi(\mathrm{HOMO})\rightarrow\pi^*(\mathrm{LUMO})$ transition character in polar solvents as well as in nonpolar solvents or the gas phase. To confirm that the S_1 FC state has the $\pi(\mathrm{HOMO})\rightarrow\pi^*(\mathrm{LUMO})$ transition character in polar solvents as well as in nonpolar solvents or the gas phase, we have performed (nonequilibrium) PCM-TDDFT(B3LYP) calculations[30] of vertical excitation energies in a nonpolar solvent of benzene and a polar solvent of DMSO at the S_0min structure optimized in vacuum (nonrelaxed) and in solvents (relaxed). Tables S1 and S2 of the SI show optimized S_0min structures and harmonic vibrational frequencies of the O1−C2(C═O) and C5−N8(C═N) stretching modes in benzene and DMSO at the PCM-B3LYP/6-31G* level, respectively. As expected, R(O1−C2) and R(C5−N8) in DMSO are longer than those in benzene, whereas R(N8−C9) and R(C12−N15) in DMSO are shorter than those in benzene, and θ(C4−C5−N8−C9) in DMSO is larger than that in benzene, whereas θ(C5−N8−C9−C10) in DMSO is smaller than that in benzene, which means that the **Z** character of the S_0 electronic structure in a polar solvent of DMSO is larger than that in a nonpolar solvent of benzene. The increase of the **Z** character of the S_0 state in DMSO can be also confirmed by the vibrational frequencies of the O1−C2(C═O) and C5−N8(C═N) stretching modes, that is, as shown in Table S2 of the SI, the theoretical and experimental vibrational frequencies of the two stretching modes in DMSO are smaller than those in benzene. Here it should be emphasized that the vibrational frequencies of the two stretching modes in benzene and DMSO calculated at the PCM-B3LYP/6-31G* level are in very good agreement with those observed by Raman shifts,[15,18] so that the description of the S_0 electronic structure of PB by the B3LYP method is considered to be fairly good. Table S3 of the SI gives the results of the PCM-TDDFT(B3LYP) calculations of vertical excitation energies in the two solvents at the S_0min structures optimized in vacuum (nonrelaxed) and the solvents (relaxed) compared with those in vacuum. In comparison with the changes from the excitation energies in vacuum to those in the two solvents, the effects of the changes from the structure in vacuum to those in the two solvents on the vertical excitation energies are small enough. Good agreement between the PCM-TDDFT(B3LYP) vertical excitation energies to the S_1 FC state and experimental values in the two solvents indicates that the TDDFT(B3LYP) excitation energies are quite reliable. The order of vertical excitation energies to the $\pi(\mathrm{HOMO})\rightarrow\pi^*(\mathrm{LUMO})$ state ($E_{\mathrm{ex}}^{\mathrm{HO}\rightarrow\mathrm{LU}}$) is $E_{\mathrm{ex}}^{\mathrm{HO}\rightarrow\mathrm{LU}}$(vacuum) > $E_{\mathrm{ex}}^{\mathrm{HO}\rightarrow\mathrm{LU}}$(benzene) > $E_{\mathrm{ex}}^{\mathrm{HO}\rightarrow\mathrm{LU}}$(DMSO), whereas that to the $n(O)\rightarrow\pi^*(\mathrm{LUMO})$ state ($E_{\mathrm{ex}}^{n(O)\rightarrow\mathrm{LU}}$) is $E_{\mathrm{ex}}^{n(O)\rightarrow\mathrm{LU}}$(DMSO) > $E_{\mathrm{ex}}^{n(O)\rightarrow\mathrm{LU}}$(benzene) > $E_{\mathrm{ex}}^{n(O)\rightarrow\mathrm{LU}}$ (vacuum), which means that the $\pi(\mathrm{HOMO})\rightarrow\pi^*(\mathrm{LUMO})$ state is relatively stabilized in polar solvents, whereas the $n(O)\rightarrow\pi^*(\mathrm{LUMO})$ state is unstabilized compared with those in the gas phase or nonpolar solvents. Therefore it can be concluded that the S_1 FC state has the $\pi(\mathrm{HOMO})\rightarrow\pi^*(\mathrm{LUMO})$ transition character even in polar solvents as well as in nonpolar solvents or the gas phase.

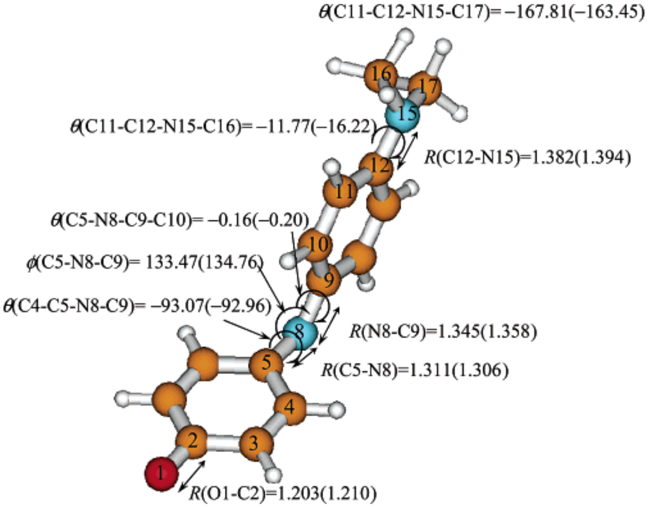

Figure 2. Structure of S_1/S_0 CImin calculated at the SA2-CASSCF(2,2)/6-31G*(6-31G(d on N/O)) level. The numbers in paretheses were results calculated using 6-31G(d on N/O).

3.2. Structure and Characterization of S_1/S_0 CImin. The structures and the energies of the minimum energy point of S_1/S_0 CI (S_1/S_0 CImin) at the SA2-CASSCF(2,2)/6-31G*(6-31G(d on N/O)) level are shown in Figure 2 and Table S4 of the SI, respectively. The significant changes between the S_0min and S_1/S_0 CImin structures particularly occur in the structural parameters related to the N8 atom: R(C5−N8), R(N8−C9), ϕ(C5−N8−C9), θ(C4−C5−N8−C9), and θ(C5−N8−C9−C10), which change from 1.270 Å, 1.392 Å, 126.3°, −10.1°, and −38.0° for S_0min to 1.311 Å, 1.345 Å, 133.5°, −93.1°, and −0.2° for S_1/S_0 CImin, respectively. It is the most characteristic of the S_1/S_0 CImin structure that the dimethylaniline ring is perpendicular to the quinoneimine ring with dihedral angles θ(C4−C5−N8−C9) ≈ −90° and θ(C5−N8−C9−C10) ≈ 0°.

We will discuss the characterization of S_1/S_0 CImin. It is well-known that near a CI point, the degeneracy of the two potential energy surfaces of I and J states is lifted for displacements in the branching (or g−h) plane, which is spanned by the energy difference gradient ($\mathbf{g}^{IJ}$) vector and the interstate coupling ($\mathbf{h}^{IJ}$) vector, whereas along all the other coordinates orthogonal to the branching plane (so-called intersection space), the degeneracy is preserved. The $\mathbf{g}^{IJ}$ and $\mathbf{h}^{IJ}$ vectors are expressed by

$$\mathbf{g}^{IJ} = \nabla(E_I - E_J) \tag{1}$$

$$\mathbf{h}^{IJ} = (E_I - E_J)\mathbf{d}_{IJ} \tag{2}$$

where E_I represents an adiabatic potential energy for an electronic state I and $\mathbf{d}_{IJ}$ denotes a nonadiabatic coupling (NADC) vector. Although the $\mathbf{g}^{IJ}$ and $\mathbf{h}^{IJ}$ vectors cannot

Chart 3

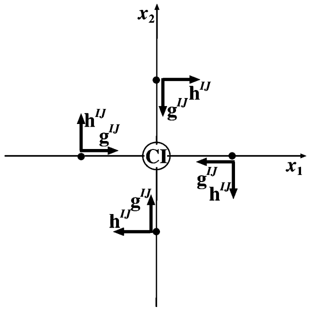

be uniquely determined at the CI point that is exactly degenerate, they can be done at a point in the branching plane displaced infinitesimally from the CI point, which is usually obtained in practice. The $\mathbf{g}^{IJ}$ and $\mathbf{h}^{IJ}$ vectors are mixed and changed depending on a position near the CI point in the branching plane due to a unitary transformation (rotation) of the two (nearly) degenerate electronic wavefunctions, which occurs when a molecule is transported along a circle centered at the CI point with an infinitesimal radius in the branching plane. Although the $\mathbf{g}^{IJ}$ and $\mathbf{h}^{IJ}$ vectors are not orthogonal to each other in general, the two vectors can be orthogonalized by a unitary transformation of the wavefunctions of the two (nearly) degenerate electronic states with rotation angles of $\beta = \beta_0 + m\pi/4$ ($m = \pm1, \pm2, ...$).[31,32] Hereafter, the orthogonalized $\mathbf{g}^{IJ}$ and $\mathbf{h}^{IJ}$ are denoted as $\mathbf{g}'^{IJ}$ and $\mathbf{h}'^{IJ}$, respectively. By using the freedom of the rotation angles, the orthogonalized ($\mathbf{g}^{IJ}$, $\mathbf{h}^{IJ}$) can be chosen as ($\mathbf{g}'^{IJ}$, $\mathbf{h}'^{IJ}$) ($m = 4n$), ($\mathbf{h}'^{IJ}$, $-\mathbf{g}'^{IJ}$) ($m = 4n + 1$), ($-\mathbf{g}'^{IJ}$, $-\mathbf{h}'^{IJ}$) ($m = 4n + 2$), and ($-\mathbf{h}'^{IJ}$, $\mathbf{g}'^{IJ}$) ($m = 4n + 3$), where $n = \pm1$, ±2, ... It should be noted that the $\mathbf{g}'^{IJ}$ and $\mathbf{h}'^{IJ}$ vectors can be interchanged by a unitary transformation of the two degenerate wavefunctions with rotation angles of $\pm\pi/4$. In the case that a certain pair of (normalized) $\mathbf{g}'^{IJ}$ and $\mathbf{h}'^{IJ}$ is employed as two bases spanning the branching plane, we represent $\mathbf{g}'^{IJ}$ and $\mathbf{h}'^{IJ}$ as $\mathbf{x}_1$ and $\mathbf{x}_2$, respectively.

Chart 3 shows variations of $\mathbf{g}^{IJ}$ and $\mathbf{h}^{IJ}$ when a system is located on the $\mathbf{x}_1$ or $\mathbf{x}_2$ axis in the close vicinity of the CI point. It is at a point in the branching plane on the minus (plus) side of the $\mathbf{x}_1$ axis displaced infinitesimally from the CI point that the $\mathbf{g}^{IJ}$ and $\mathbf{h}^{IJ}$ vectors calculated from the two (nearly) degenerate wavefunctions are directed to the $\mathbf{x}_1$($-\mathbf{x}_1$) and $\mathbf{x}_2$($-\mathbf{x}_2$) vectors, respectively. On the other hand, in the case that a molecule is located at a point in the branching plane on the minus (plus) side of the $\mathbf{x}_2$ axis diplaced infinitesimally from the CI point, the $\mathbf{g}^{IJ}$ and $\mathbf{h}^{IJ}$ vectors are directed to the $\mathbf{x}_2$($-\mathbf{x}_2$) and $-\mathbf{x}_1$($\mathbf{x}_1$) vectors, respectively.

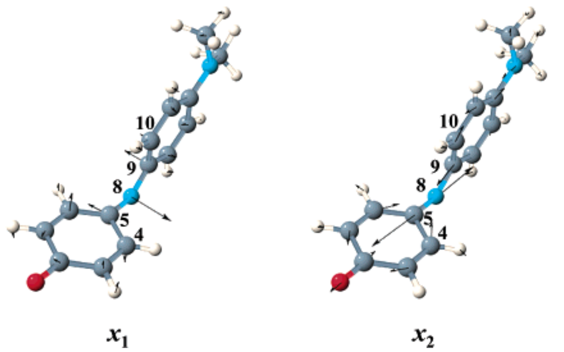

Figure 3. Directions of $\mathbf{x}_1$ and $\mathbf{x}_2$ vectors spanning the branching plane where the SA2-CASSCF(2,2)/6-31G(d on N/O) S_1/S_0 CImin point is the origin.

As derived from the degenerate perturbation theory by Yarkony,[31,32] a CI can be characterized using four conical parameters (s_x, s_y, g, and h) defined as

$$s_x = \frac{\nabla(E_0 + E_1)}{2}\cdot\mathbf{x} \tag{3}$$

$$s_y = \frac{\nabla(E_0 + E_1)}{2}\cdot\mathbf{y} \tag{4}$$

$$g = |\mathbf{g}'^{IJ}| \tag{5}$$

$$h = |\mathbf{h}'^{IJ}| \tag{6}$$

where

$$\mathbf{x} = \frac{\mathbf{g}'^{IJ}}{g} \tag{7}$$

$$\mathbf{y} = \frac{\mathbf{h}'^{IJ}}{h} \tag{8}$$

or another expression of four conical parameters useful for classification of a CI: a strength parameter ($d_{gh}^2 = (g^2 + h^2)/2$), an asymmetric parameter ($\Delta_{gh} = (g^2 - h^2)/(g^2 + h^2)$), and two tilt parameters (s_x/g and s_y/h). A point (x, y) in the branching plane can be expressed by polar coordinates as

$$x = \rho\cos\alpha \tag{9}$$

$$y = \rho\sin\alpha \tag{10}$$

In the following, the directions of the polar angles (α) of 0 and 90° are defined as those of $\mathbf{x}_1$ and $\mathbf{x}_2$, respectively.

Figure 3 shows the directions of $\mathbf{x}_1$ and $\mathbf{x}_2$ employed as bases in the branching plane, which correspond to those of the $\mathbf{g}'^{01}$ and $\mathbf{h}'^{01}$ vectors relevant to the S_1 and S_0 electronic states at the SA2-CASSCF(2,2)/6-31G(d on N/O) S_1/S_0 CImin point. The direction of $\mathbf{x}_1$ is corresponding to that of a torsional motion about the C5−N8 bond coupled with a C5−N8 bending motion in-plane of the quinoneimine ring (or a N8−C9 bending motion out-of-plane of the aniline ring), the forward and backward motion of which on the S_0 surface may lead toward the S_0min(trans) and S_0min(cis) points as will be shown later. On the other hand, $\mathbf{x}_2$ is directed to a skeletal stretching motion which has a large component of C5−N8 bond stretching motion, which leads to a bond alternation from the **Q** structure toward the **Z** one. For example, in the case that the PB molecule is located on the minus (plus) side of the $\mathbf{x}_1$ axis near the CI point in the branching plane, the $\mathbf{h}^{01}$ is directed to the $\mathbf{x}_2$($-\mathbf{x}_2$) vector and the nuclear motion along the $\mathbf{x}_2$ vector promotes a nonadiabatic transition.[39]

The SA2-CASSCF(2,2)/6-31G(d on N/O) conical parameters at the S_1/S_0 CImin point are given in Table S5 and Figure S1 of the SI shows the S_0 and S_1 potential energies in the branching plane along a circle centered at the calculated S_1/S_0 CImin point with radius $\rho = 0.01$ amu$^{1/2}$*bohr obtained from the SA2-

---

(39) In the case that the PB molecule is located on the minus (plus) side of the $\mathbf{x}_2$ axis near the CI point in the branching plane, the $\mathbf{h}^{01}$ is directed to the $\mathbf{x}_1$($-\mathbf{x}_1$) vector and the nuclear motion along the $\mathbf{x}_1$ vector promotes a nonadiabatic transition.

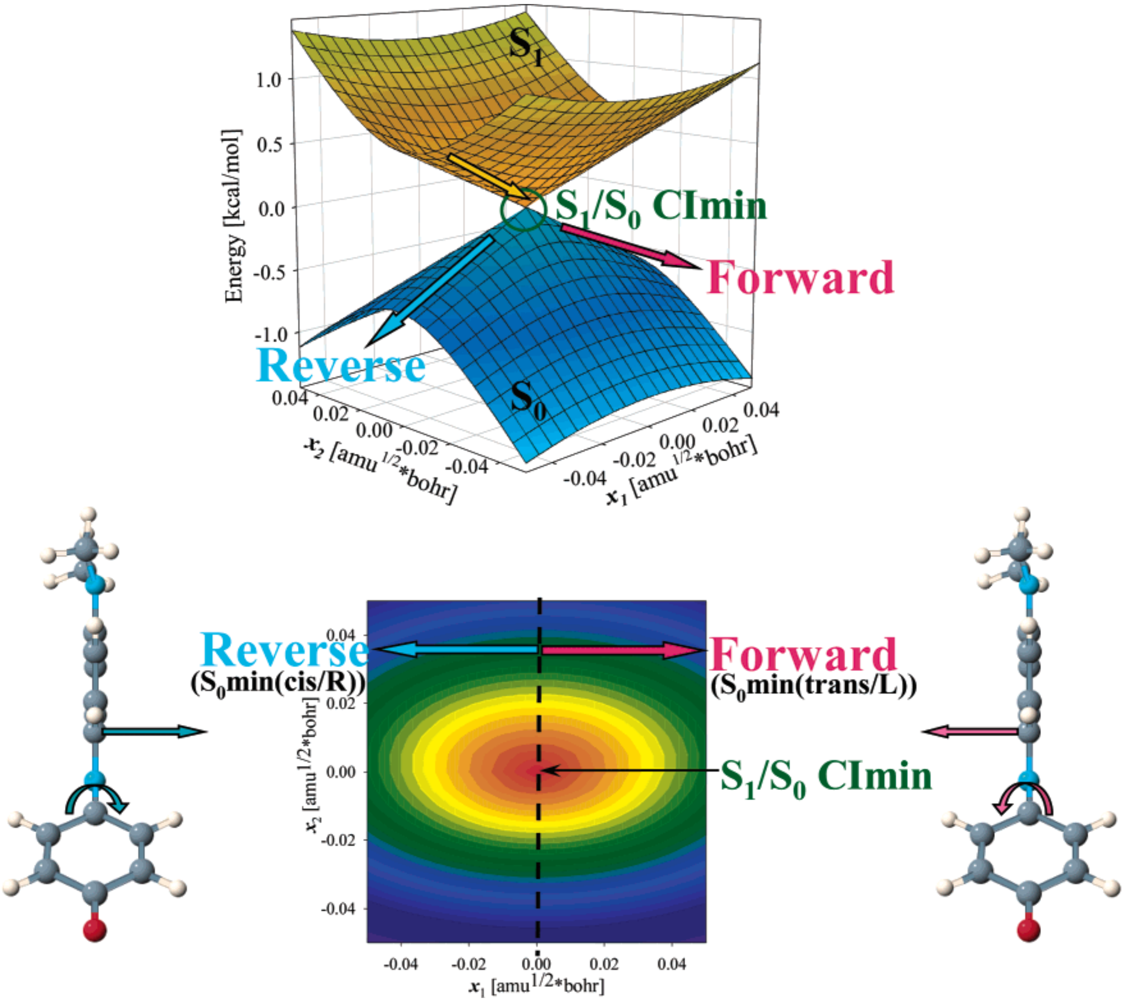

Figure 4. (Top) SA2-CASSCF(2,2)/6-31G(d on N/O) S_0 and S_1 PESs in the branching plane in the vicinity of S_1/S_0 CImin described by using the conical parameters. (Bottom) Contour of the S_0 PES. In the above two pictures, the directions into which MEPs on the S_0 surface starting from the vicinity of S_1/S_0 CImin led are indicated.

CASSCF(2,2)/6-31G(d on N/O) pointwise calculations and perturbative calculations using the conical parameters. As shown in Figure S1, the results of the pointwise calculations are so close to those of perturbative calculations that it is appropriate to discuss the S_1/S_0 CImin characterization using the conical parameters. Figure S2 of the SI represents the changes of the S_1 and S_0 wavefunctions (ConfI coefficients)[40] along a circle centered at the S_1/S_0 CImin point with radius $\rho = 0.01$ amu$^{1/2}$*bohr. We see that when transported around a closed loop in the branching plane surrounding the S_1/S_0 CImin point, both adiabatic S_1 and S_0 wavefunctions change the signs. This is so-called "electronic wavefunction phase change rule" and a necessary condition that the loop contains a CI. Figure 4 illustrates the SA2-CASSCF(2,2)/6-31G(d on N/O) S_0 and S_1 PESs in the branching plane in the vicinity of S_1/S_0 CImin described by using the conical parameters and the contour of the S_0 PES. Considering that both s_x/g and s_x/h are close to zero and $|\Delta_{gh}| \gg 0$, the S_1/S_0 CImin can be classified into a "vertical asymmetric cone" type of conical intersection,[31] which can be also confirmed in Figure 4, so that the S_1/S_0 CImin point is expected to be a branching point into two different directions (Reverse and Forward) leading to two different products (S_0min(cis) and S_0min(trans)). This will be demonstrated by minimum energy paths (MEPs) calculations from the S_1/S_0 CImin point later.

3.3. MEP on the S_1 PES Starting from the S_1 FC Point. Figure 5 shows evolutions of the S_1 and S_0 potential energies with changes of representative structural parameters along the MEP on the S_1 PES starting from the S_1 FC (S_0min(cis/R)) point (MEP$_{S_1FC}$) calculated at the SA2-CASSCF(2,2)/6-31G(d on N/O) level. To check the dynamical electron correlation effect on the SA2-CASSCF(2,2) S_1 and S_0 energy profiles and electronic characters along the SA2-CASSCF(2,2) MEP$_{S_1FC}$, we have calculated the TDDFT(B3LYP)/6-31G* energies of the four lowest singlet states along the MEP, as shown in Figure S3 of the SI. It was confirmed that along the SA2-CASSCF(2,2) MEP$_{S_1FC}$, the TDDFT(B3LYP) S_1 state remains to have the π(HOMO)→π^*(LUMO) character without any interchanges with the other state and the TDDFT(B3LYP) S_1 and S_0 energy profiles are very similar to the SA2-CASSCF(2,2) ones. Therefore, we consider that the SA2-CASSCF(2,2) calculations

---

(40) We defined $c_{\mathrm{HH}}(\mathrm{S}_i)$ and $c_{\mathrm{HL}}(\mathrm{S}_i)$ as configuration interaction (ConfI) coefficients of the S_i state with respect to two configuration state functions (CSFs): $|\mathrm{HH}\rangle = |(\mathrm{core})\phi_{\mathrm{HOMO}}\bar{\phi}_{\mathrm{HOMO}}\rangle$, which is characterized by the **Q** VB structure, and $|\mathrm{HL}\rangle=(|(\mathrm{core})\phi_{\mathrm{HOMO}}\bar{\phi}_{\mathrm{LUMO}}\rangle+ |(\mathrm{core})\phi_{\mathrm{LUMO}}\bar{\phi}_{\mathrm{HOMO}}\rangle)/\sqrt{2}$, which considerably includes the **Z** VB structure. The contribution of $|(\mathrm{core})\phi_{\mathrm{LUMO}}\bar{\phi}_{\mathrm{LUMO}}\rangle$ to the S_0 and S_1 states is zero.

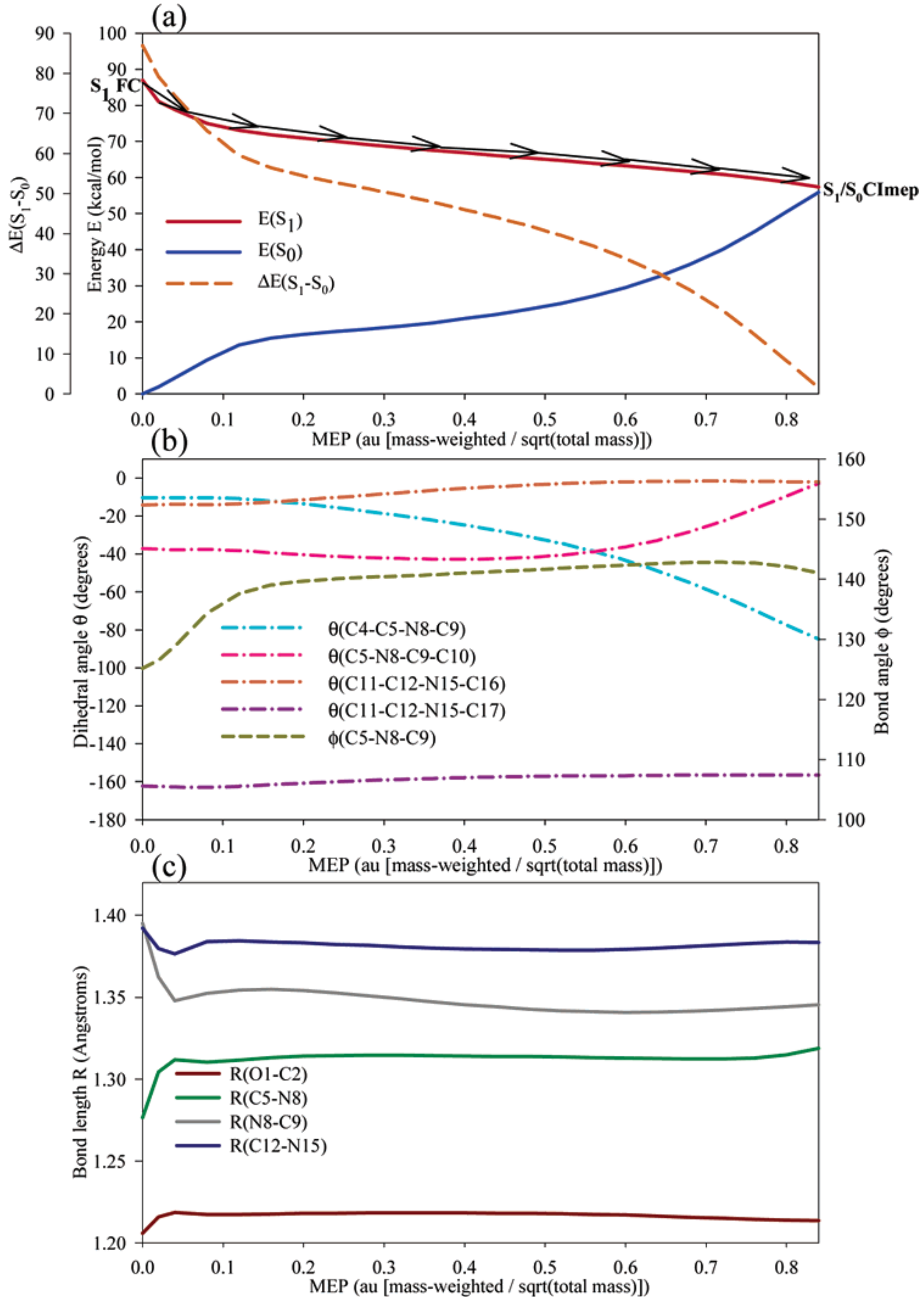

Figure 5. Reaction coordinate analysis along the MEP on the S_1 PES starting from the S_1 FC point calculated at the SA2-CASSCF(2,2)/6-31G(d on N/O) level. (a) Evolution of the S_1 and S_0 potential energies ($E(S_1)$ and $E(S_0)$) and their energy gap ($\Delta E(S_1\text{-}S_0)$). (b) Dihedral angles (θ(C4−C5−N8−C9), θ(C5−N8−C9−C10), θ(C11−C12−N15−C16), θ(C11−C12−N15−C17)) and bond angle (ϕ(C5−N8−C9)). (c) Bond lengths (R(O1−C2), R(C5−N8), R(N8−C9), R(C12−N15)).

can give a qualitatively reliable picture on the photochemical reaction of PB. In addition, to examine a solvent effect on the $\text{MEP}_{\text{S}_1\text{FC}}$, we performed the PCM-TDDFT(B3LYP)/6-31G* calculations of excitation energies in benzene and DMSO along the SA2-CASSCF(2,2) $\text{MEP}_{\text{S}_1\text{FC}}$. The profiles of the excitation energies along the SA2-CASSCF(2,2) $\text{MEP}_{\text{S}_1\text{FC}}$ in benzene and DMSO calculated by PCM-TDDFT(B3LYP), as shown Figures S4 and S5 of the SI, respectively, are similar to those in vacuum calculated by TDDFT(B3LYP) or SA2-CASSCF(2,2), which indicates that a picture of photochemical reaction dynamics from photoexcitation to decay to the S_0 state in the gas phase which will be shown later may hold true in (non)polar solvents.

Now we will discuss the static photochemical reaction pathway using the SA2-CASSCF(2,2) $\text{MEP}_{\text{S}_1\text{FC}}$, shown in Figure 5. The $\text{MEP}_{\text{S}_1\text{FC}}$ leads toward the S_1/S_0 CImin point without overcoming any barriers and can be divided into four phases.

The first phase (0.0 (S_1 FC)−0.05 au): The S_1 and S_0 potential energies show rapid decrease and increase, respectively, associated with skeletal bond stretching motions of the bond alternation from the **Q** structure toward the **Z** one and an increase of the bond angle ϕ(C5−N8−C9). The most characteristic changes in this phase are a lengthening of the C5−N8 bond due to an increase of a π^* bond character and a shortening of the N8−C9 bond due to an increase of a π bond character.

Table 5. S_1/S_0 CImep Structure Compared with the S_1/S_0 CImin Structure at the SA2-CASSCF(2,2)/6-31G(d on N/O) Level[a]

parameter	S_1/S_0 CImep[b]	S_1/S_0 CImin
R(O1−C2)	1.214	1.210
R(C5−N8)	1.319	1.306
R(N8−C9)	1.345	1.358
R(C12−N15)	1.383	1.394
ϕ(C5−N8−C9)	141.03	134.76
θ(C4−C5−N8−C9)	−84.84	−92.96
θ(C5−N8−C9−C10)	−2.85	−0.20
θ(C11−C12−N15−C16)	−1.98	−16.22
θ(C11−C12−N15−C17)	−156.44	−163.45

[a] Bond lengths are given in Å and the bond and dihedral angles are in degrees. [b] S_1 and S_0 energies are −721.694260 and −721.696526 au, respectively. $\Delta E(S_1\text{-}S_0) = 1.42$ kcal/mol. $\Delta E(\text{CImep} - \text{CImin}) = 8.02$ kcal/mol.

The second phase (0.05−0.12 au): The curvature of the S_1 energy gradually becomes smaller, whereas the S_0 energy continues to increase at the same rate as the first phase. The most characteristic change in this phase is an increase of ϕ(C5−N8−C9), whereas the changes of skeletal bond lengths are small.

The third phase (0.12−0.5 au): The S_1 and S_0 energies go down and up gradual slopes along the MEP_{S_1FC}, respectively. In this phase, the change of ϕ(C5−N8−C9) becomes moderate and instead a torsional motion about the C5−N8 bond occurs and θ(C4−C5−N8−C9) decreases from −10° due to an increase of π* character of the C5−N8 bond.

The fourth phase (0.5 au−): The S_1 energy continues to go downhill slowly, whereas an increase of the S_0 energy becomes a little steeper, and finally the energy difference between the S_0 and S_1 states ($\Delta E(S_1\text{-}S_0)$) approaches zero; that is, the MEP_{S_1FC} reaches the S_1/S_0 CI point. We call this S_1/S_0 CI as a final point of the MEP_{S_1FC}, where the energy gap $\Delta E(S_1\text{-}S_0) = 1.4$ kcal/mol, S_1/S_0 CImep, the structure of which are shown in Table 5 and later compared with S_1/S_0 CImin. With respect to the structural changes, θ(C4−C5−N8−C9) continues to decrease with a larger rate toward −90°, and in addition, a torsional motion about the N8−C9 bond occurs and θ(C5−C8-N9−C10) increases toward 0°, which may be caused by an increase of a π character in the N8−C9 bond.

Now we compare the structures of S_1/S_0 CImep and S_1/S_0 CImin. As shown in Table 5, there are non-negligible structural and energetical discrepancies between S_1/S_0 CImep and S_1/S_0 CImin. The energy of S_1/S_0 CImep is about 8 kcal/mol higher than that of S_1/S_0 CImin and there are remarkable structural differences in ϕ(C5−N8−C9) (141° for CImep and 135° for CImin) and θ(C4−C5−N8−C9) (−85° for CImep and −93° for CImin). This means that MEP_{S_1FC} leads to an energy crossing (CI) seam before reaching S_1/S_0 CImin and indicates that the discrepancy between a CI point where a system meets and the lowest energy point of a CI seam can exist even in the static nuclear motion limit.

3.4. MEPs on the S_0 PES Starting from the S_1/S_0 CImin Point. The MEPs on the S_0 PES starting from points located at $\alpha = 0-90°$ and $\alpha = 270-360°$ on a circle centered at the S_1/S_0 CImin point with radius $\rho = 0.01$ amu$^{1/2}$*bohr in the branching plane (MEP_{CI}) led to S_0min(trans/L), whereas those starting from points located at $\alpha = 90-270°$ led to S_0min(cis/R) (see Figure 4). Hereafter, we call the direction in which reaction paths bifurcate at the S_1/S_0 CI toward S_0min(cis) "Reverse"' and that toward S_0min(trans) "Forward". As shown in Figure 4, the "$\mathbf{x}_1 = 0$" line in the branching plane divides the S_0 potential energy surface into two regions which statically lead down to S_0min(cis/R) and S_0min(trans/L). As representative MEPs leading to S_0min(cis/R) and S_0min(trans/L), an MEP from a point located at $\alpha = 180°$ (MEP_{CI}(180°)), which leads to the Reverse reation (S_0min(cis/R)), is shown in Figure 6 and an MEP starting from a point located at $\alpha = 0°$ (MEP_{CI}(0°)), which leads to the Forward reaction (S_0min(trans/L)), is shown in Figure 7. The MEP_{CI}(180°) can be divided into three phases.

The first phase (0.0(S_1/S_0 CImin)−0.08 au): The S_0 and S_1 potential energies show steep decrease and increase, respectively, so that the energy gap between the S_0 and S_1 states ($\Delta E(S_1\text{-}S_0)$) becomes large rapidly. With respect to structural changes, the skeletal bond stretching motion toward the **Q** structure occurs, in which an expansion of the N8−C9 bond and a contraction of the C5−N8 bond are especially large. Simultaneously torsional motions about the C5−N8 and N8−C9 bonds occurs in which θ(C4−C5−N8−C9) increases from −90° and θ(C5−N8−C9−C10) decreases from 0°.

The second phase (0.08−0.21 au): The curvature of downhill of the S_0 energy gradually decreases, as an increase rate of θ(C4−C5−N8−C9) and a decrease rate of θ(C5−N8−C9−C10) become smaller. In addition, the N8−C9 bond continues to lengthen, whereas the other bond lengths become almost constant, and ϕ(C5−N8−C9) starts to decrease.

The third phase (0.21 au−): As ϕ(C5−N8−C9) continues to decrease until around 0.9 au, the descent line of the S_0 energy gradually become nearly flat toward the S_0min (cis/R) point, after which it becomes constant, and θ(C4−C5−N8−C9) and θ(C5−N8−C9−C10) increase very slowly.

In the MEP_{CI}(0°) leading to S_0min(trans/L), θ(C4−C5−N8−C9) decreases from −90° toward −180°, whereas θ(C5−N8−C9−C10) increases from 0 to 35°, associated with the changes of *R*(C12−N15), θ(C11−C12−N15−C16), and θ(C11−C12−N15−C17) at 1.2−1.4 au, which means that the pyramidal dimethylamine group changes like Walden-inversion. The other structural and energetical aspects of the MEP_{CI}(0°) are similar to those of MEP_{CI}(180°).

From the MEPs from the S_1 FC and S_1/S_0 CImin points, the photochemical reaction pathway of PB after photoexcitation can be schematically drawn as Figure 8.

3.5. Semiclassical Nonadiabatic Molecular Dynamics from the S_1 FC Point. We have performed the TSH nonadiabatic molecular dynamics calculations in which the electronic structure has been calculated at the SA2-CASSCF(2,2)/6-31G(d on N/O) level at each step. The trajectories were started from the S_0min(cis/R) geometry on the S_1 surface (S_1 FC) with the initial kinetic energy set zero, that is, (semi)classical motions of only a nuclear wavepacket center were followed. We consider that a sampling of initial coordinates and (nonzero) momenta from as large vibrational motions as for instance the zero point vibrations will have little effects on our results because the S_1 and S_0 PESs along the reaction coordinate are cone-shaped as shown in Figure 8, so that it can be expected that the nuclear wavepacket photoexcited to the S_1 FC point directly leads to S_1/S_0 CI with little changes of its shape and (semi)classical trajectories of the wavepacket center can be regarded as a representative of a swarm of trajectories to express a time evolution of the wavepacket.

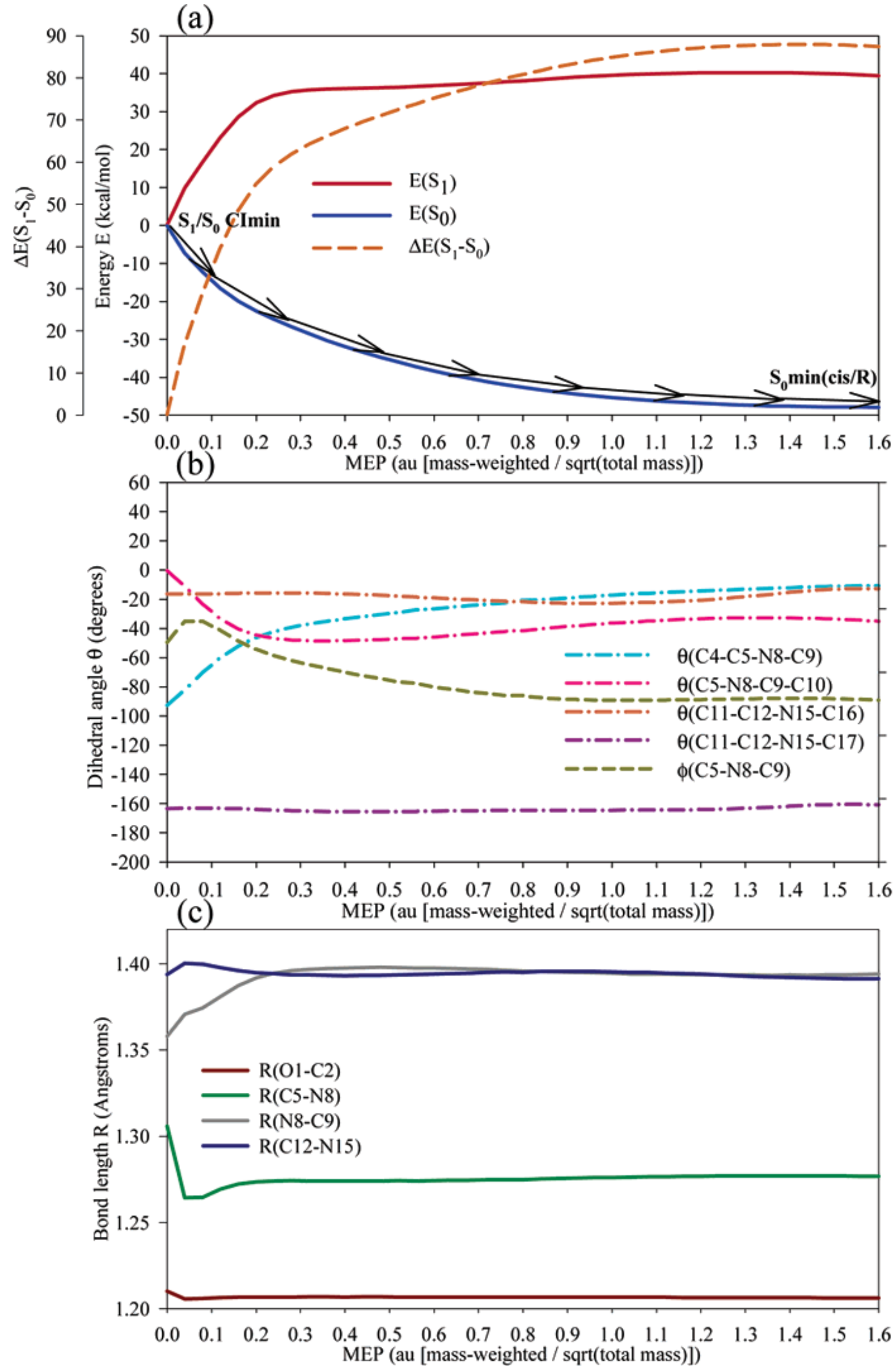

Figure 6. Reaction coordinate analysis along the MEP on the S_0 PES starting from a point 0.01 amu$^{1/2}$*bohr displaced in the direction of $\alpha = 180°$ from the S_1/S_0 CImin point calculated at the SA2-CASSCF(2,2)/6-31G(d on N/O) level. (a) Evolution of the S_1 and S_0 potential energies and their energy gap. (b) Dihedral and bond angles. (c) Bond lengths.

We discuss the calculated results of the nonadiabatic molecular dynamics by analyzing the obtained trajectories from viewpoints of two different time scales. One is a short time scale (0−250 fs) dynamics for investigating how the swarm of trajectories starting from the S_1 FC point approaches the S_1/S_0 energy crossing (CI) seam, in the vicinity of which nonadiabatic transitions efficiently occur, and bifurcate after decay to the ground state. The other is a long time scale (0−2 ps) dynamics for examining the ground state dynamics after decay, which is compared with experimental results by the PP spectroscopy.[20]

3.5.1. Short Time Scale Dynamics (0−250 fs). We have run 100 trajectories for 250 fs starting from the S_1 FC point. Table 6 shows times when surface hops have taken place, the numbers of trajectories which showed surface hops at the same time and the same propagations in the 100 trajectories, the S_1 energies, $\Delta E(S_1\text{-}S_0)$, the bond angle (ϕ(C5−N8−C9)), and the two dihedral angles (θ(C4−C5−N8−C9) and θ(C5−N8−C9−C10)) at the surface hops, compared with the S_1/S_0 CImin and CImep energies and structures, and the following paths (Reverse or Forward) into which the trajectories bifurcated. The swarm of 100 trajectories starting from the S_1 FC point showed surface

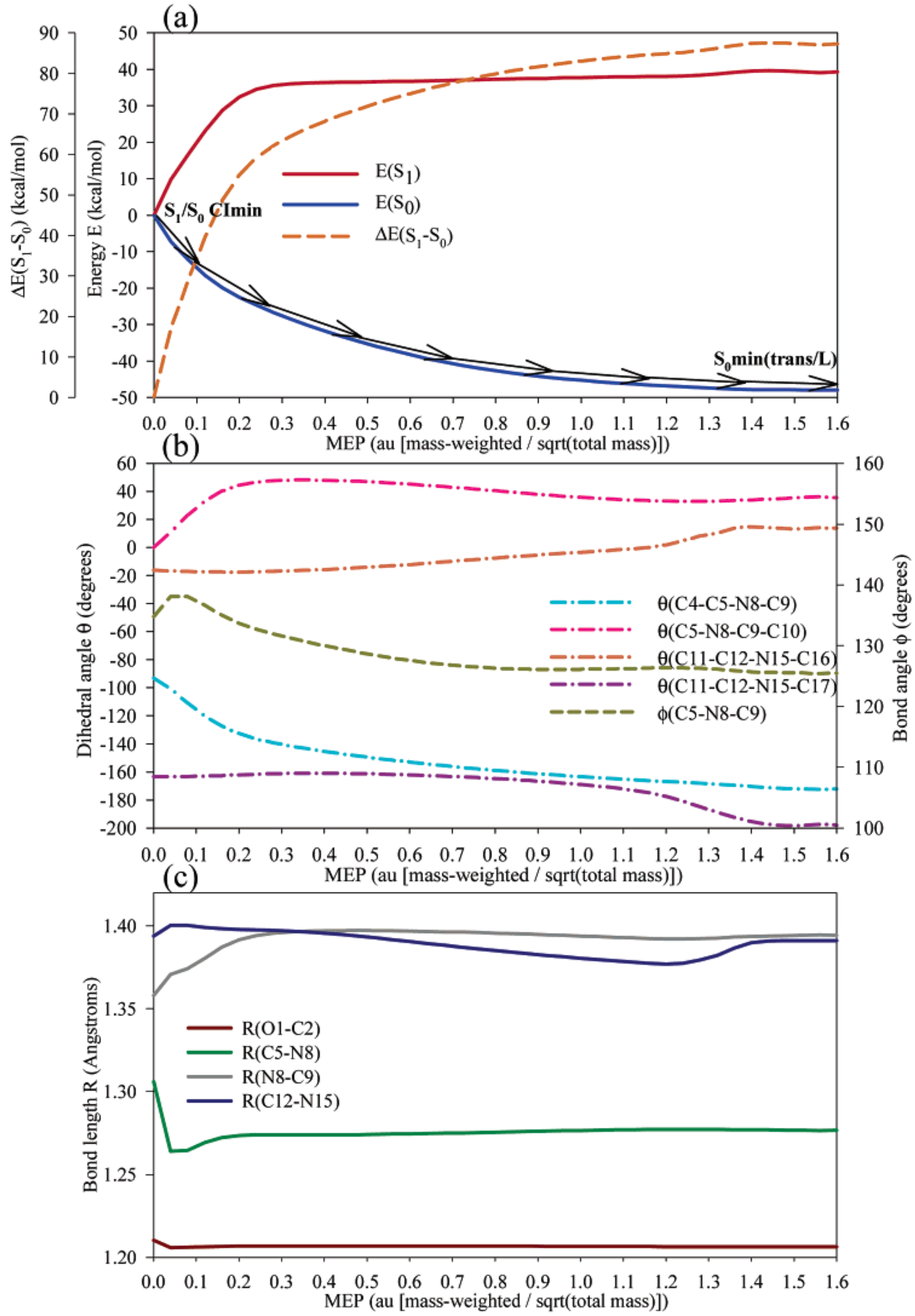

Figure 7. Reaction coordinate analysis along the MEP on the S_0 PES starting from a point 0.01 amu$^{1/2}$*bohr displaced in the direction of $\alpha = 0°$ from the S_1/S_0 CImin point calculated at the SA2-CASSCF(2,2)/6-31G(d on N/O) level. (a) Evolution of the S_1 and S_0 potential energies and their energy gap. (b) Dihedral and bond angles. (c) Bond lengths.

hops from S_1 to S_0 at 110−160 fs, in 85% of which surface hops occurred around 110−116 fs, and bifurcated into the Forward and Reverse directions with almost the same branching ratio (Reverse:Forward = 55:45). It should be emphasized that the points where surface hops have occurred are not close to the minimum energy point of conical intersection (S_1/S_0 CImin) in energies and structures. At points where surface hops occurred in the trajectories, the S_1 potential energies are 14−19 kcal/mol higher than the S_1/S_0 CImin energy, and in 85% of the trajectories, which showed surface hops around 110−116 fs, θ(C4−C5−N8−C9) range from −76 to −82°, which are more than 10° smaller in magnitude than that at S_1/S_0 CImin (−93°), and θ(C5−N8−C9−C10) are concentrated around −36°, which showed very little changes from that at S_1 FC (−37°) and are quite far from that at S_1/S_0 CImin (−0.2°). This means that before reaching the vicinity of S_1/S_0 CImin, the swarm of trajectories starting from S_1 FC enters a nonadiabatic coupling interaction region, where the nonadiabatic transition to the ground state efficiently occurs. On the other hand, the S_1/S_0 CImep point is nearer to the surface hop points in the energy and structure than S_1/S_0 CImin but there are still discrepancies especially in θ(C5−N8−C9−C10). This is an example that only a static PES information is not sufficient but a molecular dynamics simula-

Table 6. Structures at Surface Hops and Reaction Paths Following after Surface Hops in the 100 Trajectories

time (fs)	N_{traj}[a] (total = 100)	S_1 energy[b] (kcal/mol)	$\Delta E(S_1 - S_0)$ (kcal/mol)	ϕ(C5–N8–C9) (degree)	θ(C4–C5–N8–C9) (degree)	θ(C5–N8–C9–C10) (degree)	following path
110.22	7	17.01	3.79	139.97	−76.35	−37.78	Reverse
110.56	7	17.16	3.09	139.78	−76.90	−37.53	Reverse
110.79[c]	6	17.32	2.70	139.65	−77.27	−37.35	Reverse
110.98	9	17.49	2.45	139.55	−77.58	−37.20	Reverse
111.18	9	17.70	2.28	139.46	−77.89	−37.04	Reverse
113.67	1	17.33	0.51	139.10	−80.89	−35.50	Reverse
113.71	2	17.32	0.59	139.10	−80.93	−35.48	Reverse
113.77	1	17.32	0.69	139.11	−80.98	−35.46	Reverse
113.91	2	17.35	1.03	139.14	−81.10	−35.39	Reverse
114.84	1	17.74	3.30	139.25	−81.89	−35.00	Reverse
120.78	1	16.07	1.70	137.31	−84.98	−35.50	Reverse
121.32	1	15.96	1.41	136.91	−84.96	−35.98	Reverse
121.76	1	16.02	1.64	136.61	−84.85	−36.47	Reverse
133.75	1	14.70	0.91	138.53	−83.72	−36.96	Reverse
134.03[d]	2	14.69	0.39	138.71	−83.98	−36.52	Reverse
135.86	2	16.82	2.38	139.78	−85.24	−34.31	Reverse
144.82	1	18.31	3.17	138.35	−84.14	−40.10	Reverse
162.34[e]	1	17.33	1.67	128.49	−92.11	−53.67	Reverse
111.37[f]	15	17.92	2.19	139.37	−78.19	−36.89	Forward
111.57	7	18.15	2.15	139.29	−78.48	−36.73	Forward
111.80	12	18.40	2.15	139.21	−78.82	−36.55	Forward
112.08	3	18.62	2.13	139.13	−79.21	−36.35	Forward
112.42	2	18.71	2.01	139.07	−79.64	−36.12	Forward
115.12	1	17.87	3.92	139.26	−82.12	−34.89	Forward
118.77	1	18.00	5.66	138.51	−84.40	−34.59	Forward
134.11[g]	1	14.70	0.25	138.76	−84.05	−36.40	Forward
134.15	2	14.70	0.19	138.78	−84.09	−36.34	Forward
156.59	1	16.35	5.84	132.81	−94.02	−42.28	Forward
S_1/S_0 CImep		8.02	1.42	141.03	−84.84	−2.85	
S_1/S_0 CImin		0.00	0.01	134.76	−92.96	−0.20	

[a] Numbers of trajectories which showed surface hops at the same time and the same propagations. [b] Relative energies to the S_1/S_0 CImin energy. [c] This trajectory is shown in Figures 9 and 12. [d] This trajectory is shown in Figures S6 and 12. [e] In this trajectory, a surface hop from S_0 to S_1 occurred at t = 134.11 fs and that from S_1 to S_0 occurred at t = 134.28 fs. [f] This trajectory is shown in Figures 10 and 13. [g] This trajectory is shown in Figures S7 and 13.

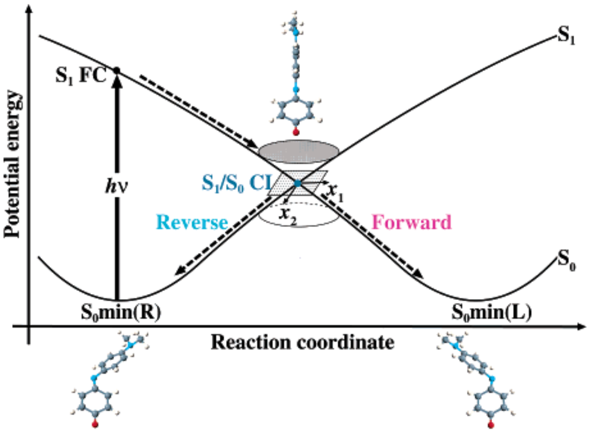

Figure 8. Schematic picture of the photochemical reaction pathway of PB.

tion is necessary to discuss the photochemical reaction mechanism.

Now we will focus on two representative trajectories leading into the Reverse and Forward reactions. Figure 9 shows a representative trajectory leading to the Reverse reaction in which a surface hop occurred at 110.79 fs, on which 6 of 100 trajectories have propagated, and Figure 10 shows a representative trajectory leading to the Forward reaction in which a surface hop occurred at 111.37 fs, on which 15 of 100 trajectories have propagated.[41] Along the trajectory propagating on the S_1 potential energy surface from starting at S_1 FC until a time when a surface hop occurs, the energy of the S_1 state decreases very gradually without overcoming any barriers, whereas the S_0 energy remarkably increases with reflections of the changes of ϕ(C5−N8−C9) and θ(C4−C5−N8−C9), so that $\Delta E(S_1\text{-}S_0)$ approaches zero. The bending motion of ϕ(C5−N8−C9) and torsional motion about the C5−N8 bond are sensitive to the S_0 energy but not to the S_1 one. The S_1 population starts to decrease from about 100 fs, when the trajectory enters a nonadiabatic coupling interaction region, and dramatically decreases at 110 fs, which means that the probability of occurrence of a surface hop (nonadiabatic transition) from S_1 to S_0 is large there.

From the viewpoint of time evolution of the structure, where the variations of the structural parameters related to the ring-bridging N8 atom are the most characteristic, the trajectories between 0 fs and a few tens of femtoseconds after the surface hops from S_1 to S_0 can be divided into four phases. Figure 11 presents snapshots of the four phases in the two representative trajectories leading to the Reverse and Forward reactions shown in Figures 9 and 10.

The first phase (0−10 fs): The skeletal bonds change toward the bond alternation to the **Z** structure where an expansion of the C5−N8 bond and a contraction of the N8−C9 bond are especially characteristic, whereas the bond angle ϕ(C5−N8−C9) increases. The dihedral angles ϕ(C4−C5−N8−C9) and θ(C5−N8−C9−C10) have shown very little changes yet.

The second phase (10−35 fs): The C5−N8 and N8−C9 bonds start to vibrate around R(C5−N8) ≈ 1.32 Å and R(N8−

---

(41) The two trajectories shown in Figures 9 and 10 are the same until 110.79 fs. The other trajectories leading to the Reverse and Forward reactions are shown in Figures S6 and S7 of the Supporting Information.

(42) Scott, A. P.; Radom, L. *J. Phys. Chem.* **1996**, *100*, 16502−16513.

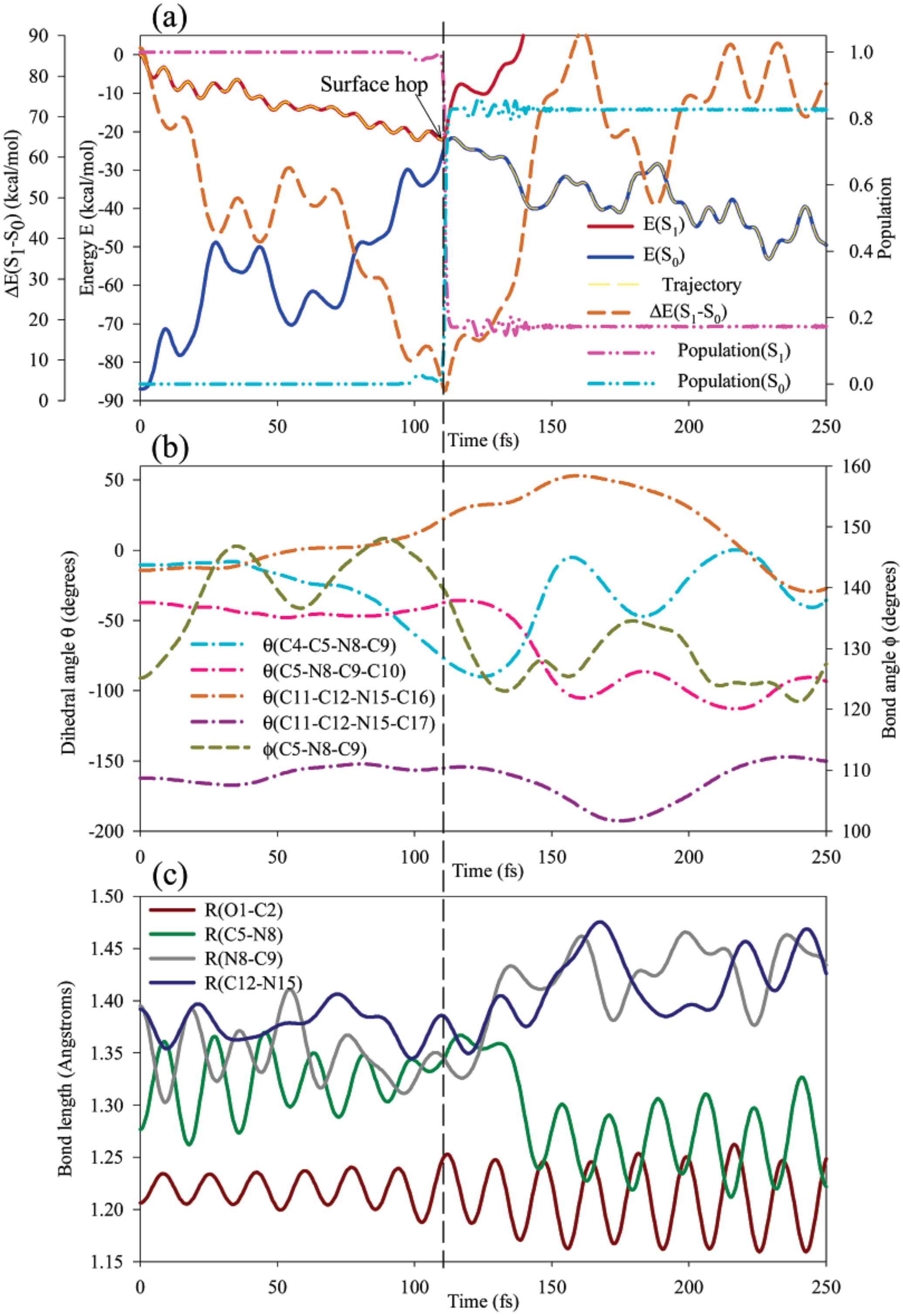

Figure 9. Representative 250 fs-trajectory starting from the S_1 FC point leading to the Reverse reaction obtained by the TSH dynamics calculation in which the electronic structure has been calculated at the SA2-CASSCF(2,2)/6-31G(d on N/O) level. (a) Evolution of the S_1 and S_0 potential energies, their energy gap, and the S_1 and S_0 populations. (b) Dihedral and bond angles. (c) Bond lengths.

C9) ≈ 1.35 Å, respectively, and ϕ(C5−N8−C9) continues to increase up to about 147°, whereas θ(C4−C5−N8−C9) and θ(C5−N8−C9−C10) still remains almost initial values.

The third phase (35 fs−surface hop): ϕ(C5−N8−C9) starts to oscillate around ϕ(C5−N8−C9) ≈ 142° with a period of about 50 fs and θ(C4−C5−N8−C9) starts to decrease. By the time that a surface hop takes place, ϕ(C5−N8−C9) vibrates twice from starting and $\Delta E(S_1\text{-}S_0)$ approaches zero gradually as θ(C4−C5−N8−C9) decreases toward −90°. On the other hand, θ(C5−N8−C9−C10) still shows very little changes from S_1 FC.

The fourth phase (surface hop−): After a surface hop from S_1 to S_0, the trajectories bifurcate into the Reverse and Forward directions. In the case of the trajectory leading to the Reverse reaction (shown in Figure 9), θ(C5−N8−C9−C10) decrease associated with the increase of θ(C4−C5−N8−C9). On the

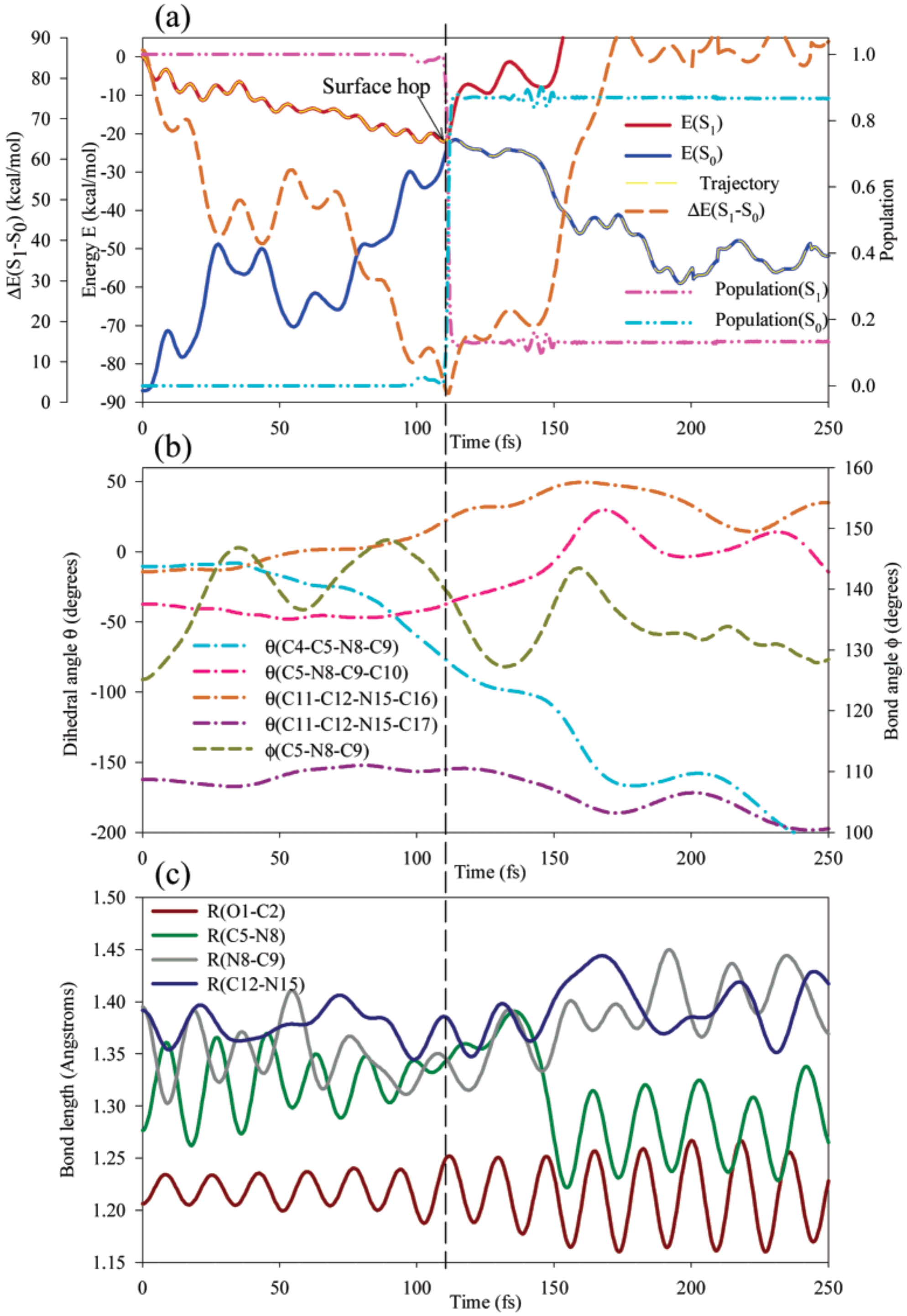

Figure 10. Representative 250 fs-trajectory starting from the S_1 FC point leading to the Forward reaction obtained by the TSH dynamics calculation in which the electronic structure has been calculated at the SA2-CASSCF(2,2)/6-31G(d on N/O) level. (a) Evolution of the S_1 and S_0 potential energies, their energy gap, and the S_1 and S_0 populations. (b) Dihedral and bond angles. (c) Bond lengths.

other hand, in the case of the trajectory leading to the Forward reaction (shown in Figure 10), θ(C5−N8−C9−C10) increase associated with the decrease of θ(C4−C5−N8−C9).

3.5.2. Long Time Scale Dynamics (0−2 ps). We will discuss a ground state recovery time and a coherently photoexcitation-induced vibrational mode after decay by comparing the results of 2 ps time scale dynamics calculations after decay to the ground state with the PP experimental results.[20] We have run four trajectories starting from S_1 FC for 2 ps, two of which lead to the Reverse reaction and the other two of which lead to the Forward reaction. Except that time scale windows are different, two trajectories shown in Figure 12 (Figure 13), which led to the Reverse (Forward) reaction, are the same as those in Figures 9 and S6 (see SI) (Figures 10 and S7 (see SI)). (It should be noted that the trajectory shown in top of Figure 13 directed to the Forward reaction after a surface hop but led to trans-PB as a product at 2 ps via a cis−trans isomerization on the ground state at about 800 fs.) In all of four trajectories θ(C4−C5−N8−C9) starts to vibrate about 0° or −180° and the ground state energy also starts to oscillate stationarily around 200−

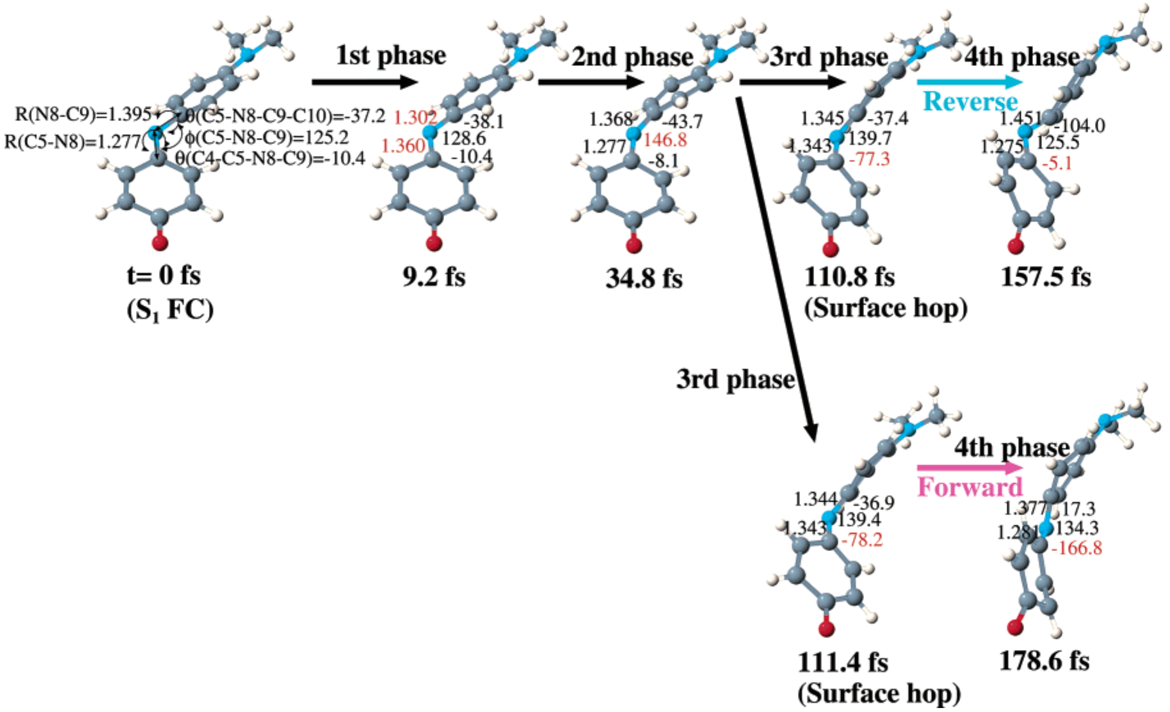

Figure 11. Snapshots of the four phases in the two representative trajectories leading to the Reverse and Forward reactions shown in Figures 9 and 10. The structural parameters the characteristic changes of which occur in each phase are written in red.

300 fs, during which the trajectories are considered to reach the vicinity of minimum energy points in the ground state. That is, the ground state recovery of PB after photoexcitation is considered to be completed around 200−300 fs, which is in good agreement with the fast time component of the ground state recovery in the PP measurement.[20] It is clear that all the other 250 fs trajectories will similarly show the ground state recovery around 200−300 fs if they run longer because the surface hops occurred during a short time range (110−160 fs).

Now we will focus on a time evolution of bond angle ϕ(C5−N8−C9) after decay to the ground state. As shown in Figures 12 and 13, the bending motions about ϕ(C5−N8−C9) with a low frequency of about 43 cm^{-1} (= a period of about 700 fs) are enhanced after decay in all of four trajectories and the variation of the S_0 energy in this time scale is corresponding to the bending motion. The vibrational phases of the bending motion of ϕ(C5−N8−C9) enhanced after decay in four trajectories are almost coherent until 800 fs, which is due to results that after impulsive photoexcitation, the bending motions of ϕ(C5−N8−C9) start simultaneously and the nonadibatic transition from S_1 to S_0 is almost completed during a short time range (110−116 fs), compared with a long time period of the ϕ(C5−N8−C9) bending vibration (700 fs). All the other 250 fs trajectories, where the bending motions of ϕ(C5−N8−C9) also start simultaneously and the nonadibatic transition from S_1 to S_0 is almost completed during a short time range, will show similar coherencies if they run longer. On the other hand, there are no coherencies in the torsional vibrations of the C5−N8 and N8−C9 bonds (θ(C4−C5−N8−C9) and θ(C5−N8−C9−C10)). After decay, the bending vibration remains coherent in two trajectories leading to the Reverse reaction (shown in Figure 12), whereas in two trajectories leading to the Forward reaction (shown in Figure 13), the vibrational coherence is disordered by energy distribution from the torsional motion about the C5−N8 bond at about 800 fs. It is considered that the coherent vibration of the bending motion about ϕ(C5−N8−C9) on the ground state induced by photoexcitation might be observed as a vibrational mode with a low frequency (about 70 cm^{-1} in aprotic solvents) in the PP measurement.[20]

4. Conclusions

We have systematically studied the photochemical reaction mechanism of phenol blue (PB) mainly based on *ab initio* CASSCF calculations using the static and dynamic approaches.

First, we have investigated the electronic states which take part in the photochemical reaction of PB after photoexcitation to the visible absorption band. It was found from the dynamical electron correlated TDDFT(B3LYP) calculations of the vertical excitation energies including a solvent effect by PCM that the lowest singlet (S_1) FC state has not an n(O)(or n(N))→π*(LUMO) character but a π(HOMO)→π*(LUMO) one in polar solvents as well as in nonpolar solvents or the gas phase and it was verified from the ((PCM-)TDDFT(B3LYP)) excited-state energy calculations including a dynamical electron correlation effect (and a solvent effect) along the SA2-CASSCF-(2,2) MEP starting at the S_1 FC point that the π(HOMO)→π*(LUMO) (S_1) state with the **Z**-like character and the S_0 states with the **Q** character take part in the photochemical reaction of PB.

From the SA2-CASSCF(2,2) MEPs calculations and the nonadiabatic *ab initio* molecular dynamics simulations, we found that the photochemical reaction path starting at the S_1 FC point barrierlessly leads to the S_1/S_0 CI point, where the reaction path bifurcates into two (Reverse and Forward) directions and the motions of the $\mathbf{x}_1$ (a skeletal stretching motion leading to a bond alternation from the **Q** structure toward the **Z** one) or $\mathbf{x}_2$ (a torsional motion about the C5−N8 bond coupled with a C5−N8 bending motion in-plane of the quinoneimine ring) directions promote the nonadiabatic transition.

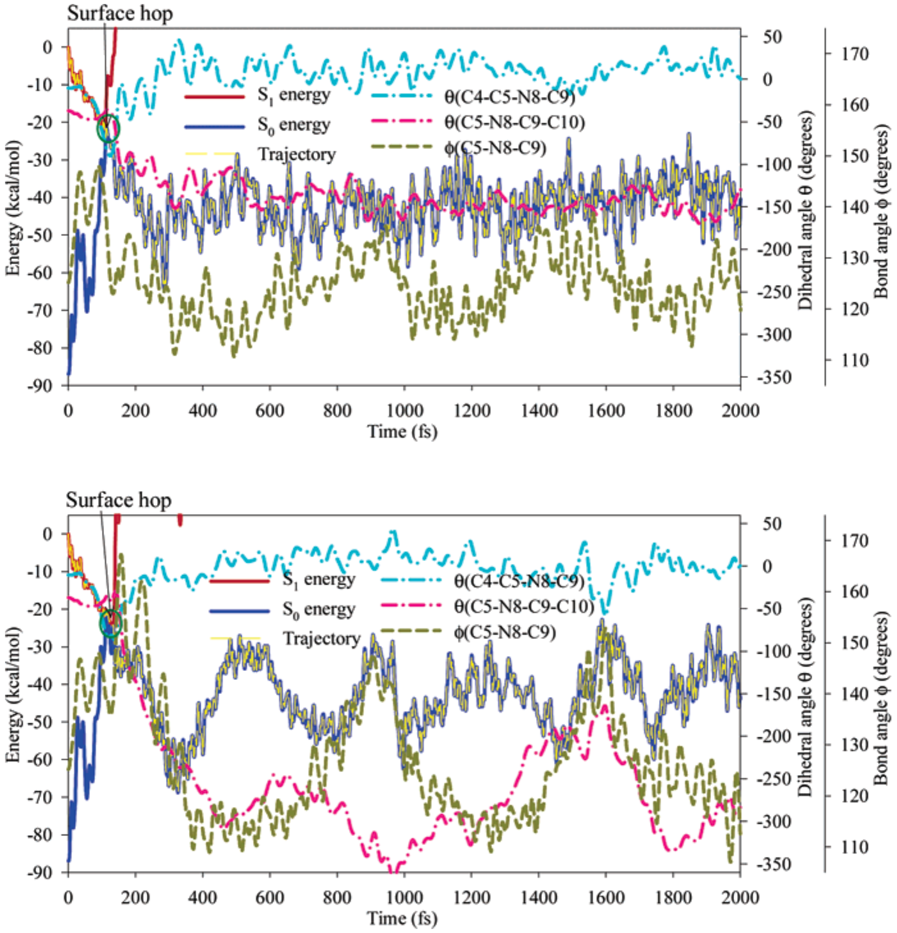

Figure 12. Time evolution of the S_1 and S_0 potential energies, the dihedral angles (θ(C4−C5−N8−C9), θ(C5−N8−C9−C10)), and the bond angle (ϕ-(C5−N8−C9)) along the 2 ps-trajectories starting from the S_1 FC point leading to the Reverse reaction obtained by the TSH dynamics calculation in which the electronic structure has been calculated at the SA2-CASSCF(2,2)/6-31G(d on N/O) level. The trajectories shown in the upper and lower figures correspond to those in Figures 9 and S6, respectively.

It was also found from the nonadiabatic molecular dynamics simulations that the photochemical reaction path can be divided into four phases: In the first phase, a stretching motion of the skeletal bonds toward the bond alternation to the **Z** structure occurs. In the second phase, an increase of ϕ(C5−N8−C9) is characteristic. In the third phase, a torsional motion about the C5−N8 double bond occurs toward θ(C4−C5−N8−C9) = −90° and the swarm of the TSH trajectories starting at the S_1 FC point mostly has showed the nonadiabatic transition from S_1 to S_0 at 110−116 fs in the vicinity of S_1/S_0 CI. In the fourth phase, after decay to the S_0 state, the swarm of the TSH trajectories bifurcated into the Forward and Reverse directions with almost the same branching ratio. It should be emphasized that the points where surface hops (nonadiabatic transitions) have occurred in the TSH trajectories are not close to the S_1/S_0 CImin (even CImep) point in energies and structures, which indicates that only a static PES information is not sufficient but a molecular dynamics simulation is necessary to discuss the photochemical reaction mechanism of PB.

All of the 2 ps trajectories have reached the vicinity of minimum energy points in the ground state around 200−300 fs, which is in good agreement with the fast time component of the ground state recovery in the PP measurement. Therefore, we consider that the mechanism of the photochemical reaction of PB which we have shown is quite reliable. Furthermore, coherent vibrations of the bending motion about the bond angle between two rings of PB with a low frequency (43 cm^{-1}) have been induced after decay to the ground state, which might be observed as a low-frequency vibrational mode in the PP measurement. The mechanism shown in this work is expected to hold good for the photochemical reaction of not only PB but also its similar organic dyes having such a primary skeletal structure as shown in Chart 4, e.g. indoaniline, indophenol, and indonaphthol dyes.

In this study, nonadiabatic *ab initio* molecular dynamics simulations of the ultrafast photochemical reaction of PB have been performed in the gas phase, so that we have successfully obtained important information on the fast decay component and the coherently photoexcitation-induced vibrational mode with a low frequency of PB observed by the PP transient absorption spectroscopy. Another interesting subject on photochemistry or photophysics of PB is about an origin of the slow decay components of the PP signal, which is considered to be due to solvation dynamics, vibrational cooling, and/or structural relaxation strongly caused or influenced by intermolecular interactions between the PB molecule and surrounding solvents. It would be possible to elucidate the origin of the slow decay components of the PP signal by an *ab initio* nonadiabatic dynamics simulation including an explicit solvent effect such as a quantum mechanics/molecular mechanics (QM/MM) molecular dynamics, which is a future work.

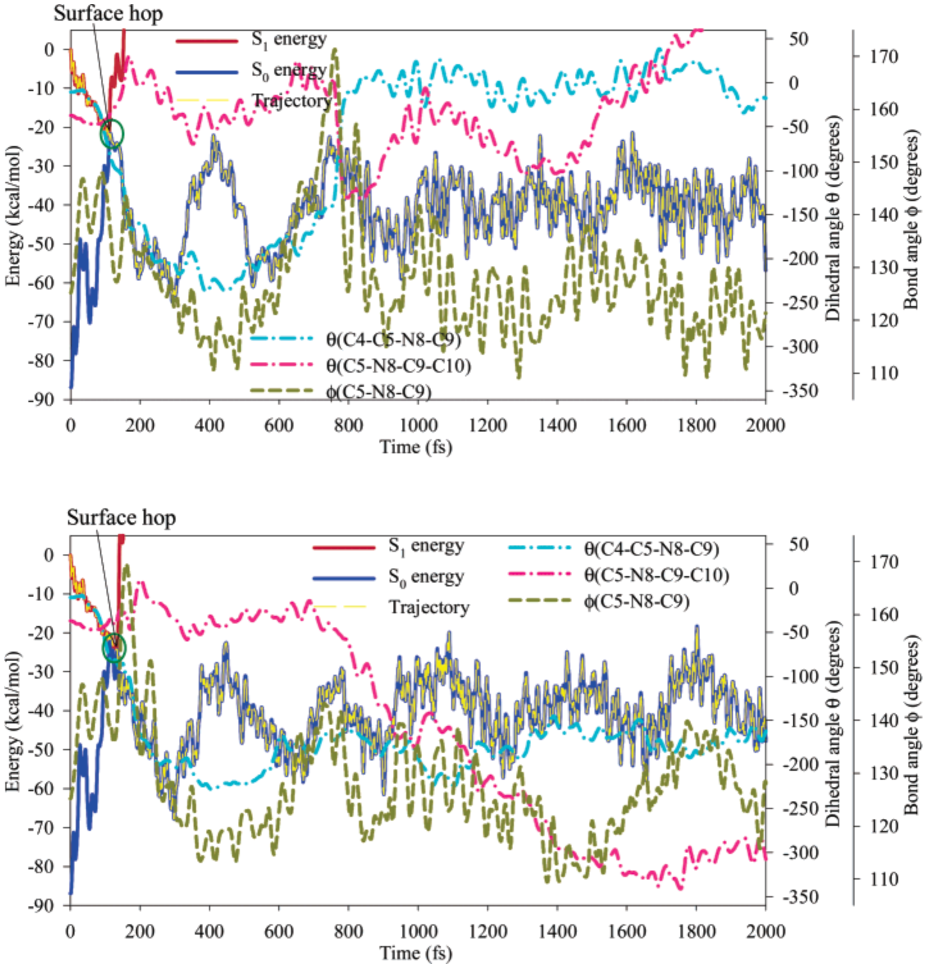

Figure 13. Time evolution of the S_1 and S_0 potential energies, the dihedral angles (θ(C4−C5−N8−C9), θ(C5−N8−C9−C10)), and the bond angle (ϕ-(C5−N8−C9)) along the 2 ps-trajectories starting from the S_1 FC point leading to the Forward reaction obtained by the TSH dynamics calculation in which the electronic structure has been calculated at the SA2-CASSCF(2,2)/6-31G(d on N/O) level. The trajectories shown in the upper and lower figures correspond to those in Figures 10 and S7, respectively.

Chart 4 [a]

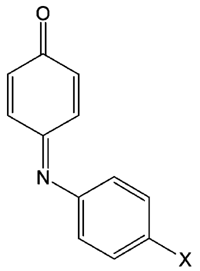

[a] X = substituent such as NR_2 or OR (R: H, alkyl group).

Acknowledgment. We are so grateful to Prof. Y. Nagasawa in Osaka University for giving us useful experimental information of PB. We also thank Prof. S. Yabushita in Keio University for fruitful discussions about the characterization of conical intersections. We appreciate Prof. M. Olivucci in Universita di Siena for giving us good suggestions. This work was supported by CREST of Japan Science and Technology Agency (JST).

Supporting Information Available: Chart S1 for the cis/trans and R/L forms of S_0min of PB. Table S1 for the optimized S_0-min structures of PB in benzene and DMSO at the PCM-B3LYP/6-31G* level. Table S2 for the vibrational frequencies of the O1−C2(C═O) and C5−N8(C═N) stretching modes of PB in benzene and DMSO at the PCM-B3LYP/6-31G* level. Table S3 for the vertical excitation energies from the S_0 state to three lowest singlet Franck-Condon excited states of PB in benzene and DMSO at the PCM-TDDFT(B3LYP)/6-31G* level. Table S4 for the energies of S_1/S_0 CImin of PB at the SA2-CASSCF(2,2) level. Table S5 for the conical parameters of S_1/S_0 CImin of PB. Figures S1 and S2 for the potential energies and the ConfI coefficients of the S_0 and S_1 states in the branching plane along a circle centered at the S_1/S_0 CImin point, respectively. Figure S3 for the TDDFT(B3LYP)/6-31G* energy profiles of the four lowest singlet states along the SA2-CASSCF-(2,2)/6-31G(d on N/O) $\mathrm{MEP}_{\mathrm{S_1FC}}$ in vacuum. Figures S4 and S5 for the PCM-TDDFT(B3LYP)/6-31G* energy profiles of the four lowest singlet states along the SA2-CASSCF(2,2)/6-31G(d on N/O) $\mathrm{MEP}_{\mathrm{S_1FC}}$ in benzene and DMSO, respectively. Figure S6 for the other representative 250 fs-trajectory leading to the Reverse reaction than that shown in Figure 9. Figure S7 for the other representative 250 fs-trajectory leading to the Forward reaction than that shown in Figure 10. Cartesian coordinates of the optimized structures. Tables S6−S13 for the S_0min structures of PB optimized at the SA2-CASSCF(2,2), HF, MP2, and B3LYP levels. Tables S14−S18 for the S_0min structures of TEYGOT optimized at the HF, MP2, and B3LYP levels. Tables

S19 and S20 for the SA2-CASSCF(2,2) S_1/S_0 CImin structures obtained with 6-31G* and 6-31G(d on N/O) basis sets, respectively. Table S21 for the SA2-CASSCF(2,2)/6-31G(d on N/O) S_1/S_0 CImep structures. Tables S22 and S23 for the S_0-min structures of PB in benzene and DMSO optimized at the PCM-B3LYP/6-31G* level, respectively. Complete refs 33 and 35. This material is available free of charge via the Internet at http://pubs.acs.org.

JA066994W